

On the Performance of In-Body RF Localization Techniques

A Thesis submitted to the faculty of

WORCESTER POLYTECHNIC INSTITUTE

In partial fulfillment of the requirement for the degree of

Master of Science

in

Electrical and Computer Engineering

By



Pranay P. Swar

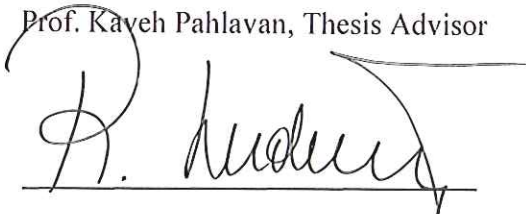
(pranay.swar@wpi.edu)

May 30th, 2012

APPROVED:



Prof. Kaveh Pahlavan, Thesis Advisor



Prof. Reinhold Ludwig, Graduate Program Coordinator, ECE

Abstract

Localization inside the human body using Radio Frequency (RF) transmission is gaining importance in a number of applications such as Wireless Capsule Endoscopy. The accuracy of RF localization depends on the technology adopted for this purpose. The two most common RF localization technologies use Received Signal Strength (RSS) and Time-Of-Arrival (TOA). This research first provides bounds for accuracy of localization of a Endoscopy capsule inside the human body as it moves through the gastro-Intestinal track with and without randomness in transmit power using RSS based localization with a triangulation algorithm. It is observed that in spite of the presence of a large number of anchor nodes; the localization error is still in range of few cm, which is quite high; hence we resort to TOA based localization. Due to lack of a widely accepted model for TOA based localization inside human body we use a computational technique for simulation inside and around the human body, named Finite Difference Time Domain (FDTD). We first show that our proprietary FDTD simulation software shows acceptable results when compared with real empirical measurements using a vector network analyzer. We then show that, the FDTD method, which has been used extensively in all kinds of electromagnetic modeling due to its versatility and simplicity, suffers seriously because of its demanding requirement on memory storage and computation time, which is due to its inherently recursive nature and the need for absorbing boundary conditions. In this research we suggest a novel computationally efficient technique for simulation using FDTD by considering FDTD as a Linear Time Invariant (LTI) system. Then we use the software to simulate the TOA of the narrowband and wideband signals propagated inside the human body for RF localization to compare the accuracies of the two using this method.

Table of Contents

Abstract.....	02
Table of Contents.....	03
List of Figures and Tables.....	05
Glossary.....	08
Acknowledgment.....	10
Chapter 1: Introduction.....	11
1.1 Background of Research.....	11
1.1.1 Body Area Network: an overview.....	11
1.2 Motivation of Research.....	17
1.3 Contribution to the Thesis.....	18
1.4 Summary of the Chapters in the Thesis.....	19
Chapter 2: Body Area Network and localization.....	20
2.1 Localization.....	21
2.2 Localization techniques.....	21
2.2.1 Distance measurement using received signal strength.....	22
2.2.2 Round trip propagation time measurements.....	23
2.2.3 Time difference of arrival measurements.....	25
2.3 Challenges in Localization for Body area network.....	26
2.3.1 Non-Homogeneity.....	27
2.3.2 Movement of the body.....	29

2.4 Antenna Effect.....	30
2.5 Electrical Properties of Human body.....	31
Chapter 3: Performance Bounds for Wireless Capsule Endoscopy with Random Transmit Power	
3.1 Wireless Capsule Endoscopy.....	33
3.2 Localization in Wireless Capsule Endoscopy.....	36
3.3 Randomness in Transmit Power.....	38
3.4 Channel model for Body Area network.....	39
3.5 Derivation of the Bayesian Cramer Rao bound.....	42
3.6 Analysis of the Bounds.....	49
3.6.1 Problem Formulation and Simulation Scenario.....	49
3.6.2 Performance Bounds in different Organs.....	52
3.6.3 Performance as a function of number of sensors.....	55
3.6.3 Performance as a Function of ρ and σ_{Π}	56
Chapter 4: Fast FDTD Simulation Techniques for analysis of TOA based Localization.....	58
4.1 Introduction.....	58
4.2 FDTD for waveform Transmission.....	60
4.2 Comparison of Waveform Simulation with Measurements.....	68
4.3 Computational Complexity.....	75
4.4 Fast solution to FDTD using LTI Analysis.....	77
4.5 Efficient TOA based Localization for BANs.....	80
4.5.1 Simulation Bandwidth as a function of Distance.....	80
4.5.2 TOA accuracy as a function of Bandwidth.....	83
Chapter 5: Conclusions and Future Work.....	86
References.....	89
Appendix.....	99

List of Figures

Figure 1: Example of intra-body and extra-body communication in a WBAN.	14
Figure 2: Positioning of a Wireless Body Area Network in the realm of wireless networks . . .	15
Figure 3: Localization using time-difference-of-arrival measurements	25
Figure 4: The human Gastro-Intestinal Track	34
Figure 5: a) The wireless endoscopy capsule b) The capsule moving through GI track	35
Figure 6: Plot showing the decrease in the gain of the antenna when the antenna is placed on the surface of the body	39
Figure 7: Simplified Diagram of the simulation setup (Top View of the human body with jacket sensor planes)	50
Figure 8: Three Sensor configurations considered for analysis of the bounds (Number of sensors = 64)	51
Figure 9: Localization Performance of different configurations as a function of number of sensors	52
Figure 10: Comparison of Bayesian CRB on $1-\sigma$ uncertainty ellipses (left: Stomach Middle: Small Intestine Right: Large Intestine) when transmitted power are perfectly known (Solid line in red) or random with $\sigma_{\Pi} = 10\text{dBm}$. (Dashed lines in Black), for different unknown capsule locations (.).	54
Figure 11: Localization performance (RMSE) as a function of number of receiver sensors in different organs ($\sigma_{\text{dB}} = 7.85$ and $\alpha = 4.26$)	56

Figure 12: Bayesian CRB bounds for σ_r for 64 sensor configuration for two values of σ_{Π} and a range of ρ ($\sigma_{dB}= 7.85$ and $\alpha = 4.26$)	57
Figure 13: Yee Grid	65
Figure 14: Input signal of 84MHz to the simulation setup	69
Figure 15: The result of simulation after inputting the 84MHz ISM band signal	69
Figure 16: Input signal of 700 MHz to the simulation setup	70
Figure 17: The result of simulation after inputting the 700 MHz band signal	70
Figure 18: Input signal of 1GHz to the simulation setup	71
Figure 19: The result of simulation after inputting the 1GHz band signal	71
Figure 20: Picture of scanned and physical Phantom Mesh and dipole antennas	72
Figure 21: Comparison of Simulation and Measurement with antennas placed in front of phantom	73
Figure 22: Comparison of Simulation and Measurement with antennas placed in front and back of phantom	74
Figure 23: Computational time against grid size	76
Figure 24: LTI system	77
Figure 25: FDTD as Linear Time Invariant system	79
Figure 26: Simulation Scenario	81
Figure 27: Simulation Bandwidth for distance of 8cm (up) and 16cm (down) inside human body	82
Figure 28: Operational Bandwidth vs. distance	83
Figure 29: TOA accuracy for narrow band	84
Figure 30: TOA accuracy for Wideband	85

List of Tables

Table I: Schematic overview of differences between Wireless Sensor Networks and Wireless Body Area Networks.....	16
Table II: Electrical Properties of different tissues in Human body.....	32
Table III: Parameters for the Statically Implant To Body Surface Path Loss Model.....	41
Table IV: Percentage Increase in the RMSE (mm) of the Capsule in Three Different Organs of the GI Track.....	54
Table V: Computational Complexity and relative ratio.....	76

Glossary

ABC	Absorption Boundary Condition
BAN	Body Area Network
CEM	Computational Electromagnetics
CFL	Courant-Friedrichs-Lewy
CRB	Cramér–Rao bound
ECG	Electrocardiogram
FDA	Food and Drug Administration
FDTD	Finite Difference Time Domain
GI	Gastro-Intestinal
ISM	Industrial Scientific Medical
LED	Light Emitting Diode
LI	Large Intestine
LTI	Linear Time Invariant
MAC	Medium Access Control
MICS	Medical Implant Communication Service
NIST	National Institute of Science and Technology
PAR	Project Authorization Request
RCB	Radiation Boundary Conditions
RF	Radio Frequency
RMSE	Root Mean Square Error
RSS	Received Signal Strength

SAR	Specific Absorption Rate
TDOA	Time Difference of Arrival
TOA	Time of Arrival
UWB	Ultra Wide Band
WBAN	Wireless Body Area Networks
WCE	Wireless Capsule Endoscopy
WPAN	Wireless Personal Area Network
WLAN	Wireless Local Area Network
WSN	Wireless Sensor Network

Acknowledgments

First and foremost I offer my sincerest gratitude to my supervisor, Prof. Kaveh Pahlavan, who has supported me throughout my thesis with his patience and knowledge whilst allowing me the room to work in my own way. I attribute the level of my Master's degree to his encouragement and effort and without him this thesis, too, would not have been completed or written. One simply could not wish for a better or friendlier supervisor.

I would like to thank Prof. Allen Levesque, Dr. Kamran Sayrafian and Dr. Ning yang for their guidance and thought provoking comments during my research.

I am very grateful to Kaveh Ghaboosi, who as a good friend was always willing to help and give his best suggestions. I would never forget him for his invaluable teachings and encouragement during the early days of my research.

I would also like to thank my lab peers Yunxing Ye, Umair Khan, Ruijun Fu, Jai He, and Shin Li for providing me all the help when needed and for keeping such a friendly atmosphere in the lab.

I am very thankful to all my friends especially, Amit Sail, M. Monirul Islam, Tanmay Bhagwat, and Maitreya Bhakal, who have been my biggest support system at times of difficulties.

I would like to dedicate this work to my parents and siblings whose prayers, love and support was the ultimate motivation during my academics

Chapter 1

Introduction

1.1 Background of Research

1.1.1 Body Area Networks: an overview

Recent advancements in electronics have enabled the development of small and intelligent medical sensors devices which can be worn on or implanted inside the human body. These sensors are able to send and receive as well as analyze and store the wirelessly transmitted data. Use of a wireless interface for such electronic devices is found to be efficient relative to wired connection which turns out to be cumbersome. Another advantage is that patient experiences a greater physical mobility and is no longer compelled to stay within a hospital. This whole process is considered to be the next step in mobile health innovation, enhancing personal health care and coping with the cost of current health care; this whole technology is called mobile health

or m-health, a step further from e-health which dealt with health care practice supported by electronic processes and communication. To fully exploit the benefits of m-health a new area of specialization in wireless networks emerged, named Wireless Body Area Networks (WBANs). This term was coined by Van Dam et al. in 2001 [77]

Started as a Study Group in 2006 and motivated by the increasing research and industry interest in WBANs, the IEEE Standards Association decided to form the IEEE 802.15 Task Group 6 in November 2007. A Body Area Network (BAN) or WBAN is formally defined by IEEE 802.15 as, "a communication standard optimized for low power devices and operation on, in or around the human body (but not limited to humans) to serve a variety of applications including medical, consumer electronics personal entertainment and other" [1]. In more common terms, a Body Area Network is a system of devices in close proximity to a person's body that cooperate for the benefit of the user.

Project Authorization Request (PAR) 07-0575 presents an extended description of the task group [2]. It stresses the fact that current Wireless Personal Area Networks (WPANs) do not meet medical communication guidelines, because of the proximity to human tissue. Moreover, WPAN technology is said not to support Quality of Service, low power operation and noninterference, all required when supporting WBAN applications. Based on the responses to the Call for Applications [3], the PAR also outlines a large number of applications that can be served by the proposed standard, ranging from classical medical usage, e.g. EEG and ECG monitoring, to personal entertainment systems. In 2008, a Call for Proposals on physical layer and MAC layer protocols was issued [4]. The large number of responses, 64 in total, confirmed the industry interest. Currently, the responses are being evaluated at monthly meetings, while some proposals

are merged. The creation of the IEEE 802.15 Task Group 6 and the work on an IEEE 802.15.6 standard stresses the importance of the research with respect to WBANs.

A wireless body area network consists of sensors with small antennas intelligent enough to communicate with each other providing continuous health monitoring of the different sensing devices placed inside or on the body of the monitored patient, to the remote stations. Examples include sensors measuring the heartbeat, body temperature or recording a prolonged electrocardiogram (ECG). Other than sensors, other devices that are part of this technology are actuators that take some specific actions according to the data received from the sensors or through interaction with the users. As an example, an actuator equipped with a built in reservoir and pump administers the correct dose of insulin to a diabetic patient based on the glucose level measurements.

The development and research in the domain of WBANs is still at an early stage. As a consequence, the terminology is not always clearly defined. In the literature, protocols developed for WBANs can range from communication between the sensors on the body to communication from a body node to a data center connected to the Internet. In order to have clear understanding, the literature has suggested the following definitions: intra-body communication and extra-body communication. Doing so, the medical data from the patient at home can be evaluated by a physician or stored in a medical database. This segmentation is similar to the one defined in [5] where a multi-tiered telemedicine system is presented. Tier 1 encompasses the intra-body communication, tier 2 the extra-body communication between the personal device and the Internet, and tier 3 represents the extra-body communication from the Internet to the medical server. The combination of intra-body and extra-body communication can be seen as an enabler for ubiquitous health care service provisioning.

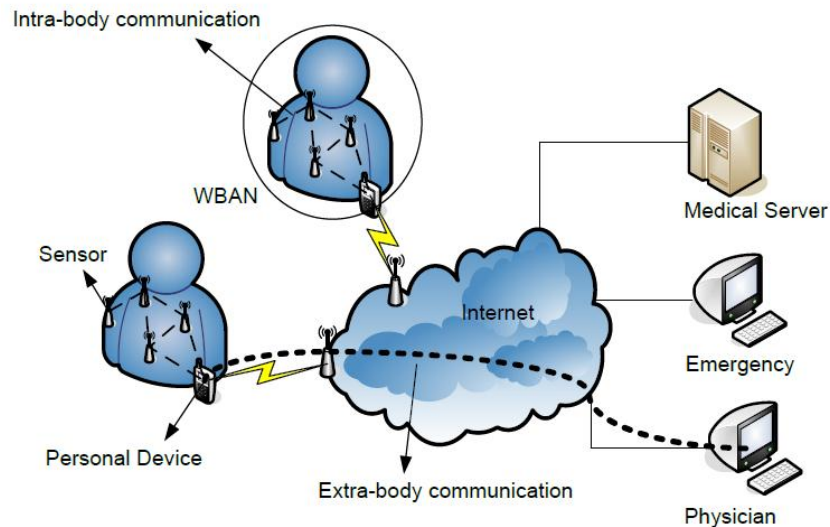


Figure 1: Example of intra-body and extra-body communication in a WBAN [1].

In Figure 2, a WBAN is compared with other types of wireless networks, such as WPAN, Wireless Local Area Network (WLAN), Wireless Metropolitan Area Network (WMAN) and Wide Area Networks (WAN) [6]. A WBAN operates close to the human body and its communication range will be restricted to a few meters, with typical values around 1-2 meters. While a WBAN is devoted to interconnection of one person's wearable devices, a WPAN is a network in the environment around the person. The communication range can be as much as 10 meters for high data rate applications and up to several 10's of meters for low data rate applications. A WLAN has a typical communication range up to hundreds of meters. Each type of network has its typical enabling technology, defined by the IEEE. A WPAN uses IEEE 802.15.1 (Bluetooth) or IEEE 802.15.4 (Zig-Bee), a WLAN uses IEEE 802.11 (WiFi) and a WMAN IEEE 802.16 (WiMax). The communication in a WAN can be established via satellite links

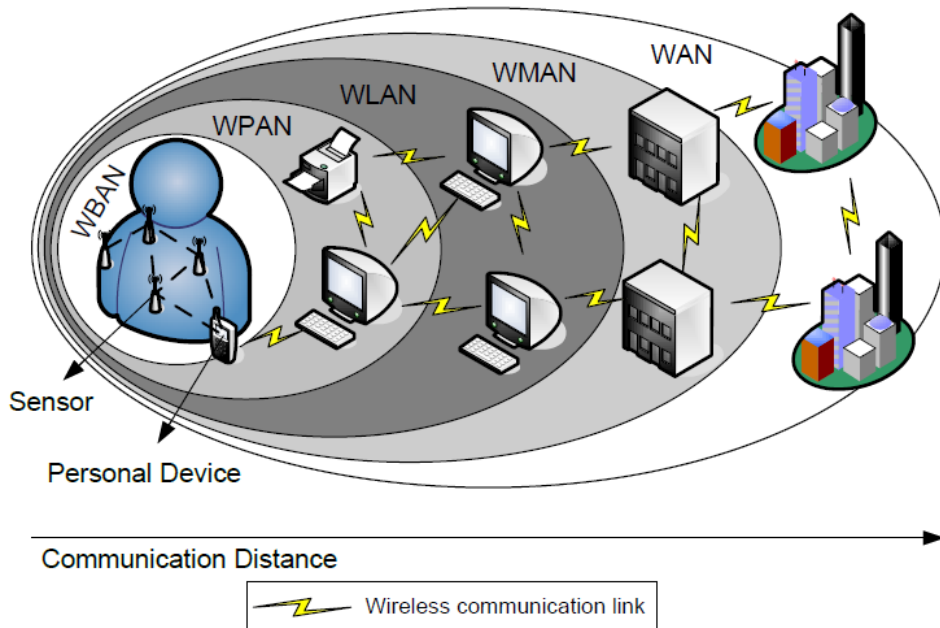


Figure 2: Positioning of a Wireless Body Area Network in the realm of wireless networks [1].

In order to realize communication between WBAN devices and sensors, techniques from Wireless Sensor Networks (WSNs) and ad hoc networks could be used. However, because of the typical properties of a WBAN, current protocols designed for those networks are not always well suited to support a WBAN. Table I summarizes the differences between these two technologies [7].

Table I: Schematic Overview of Differences Between Wireless Sensor Networks and Wireless Body Area Networks, based on [7].

Challenges	Wireless Sensor Network	Wireless Body Area Network
Scale	Monitored environment (meters / Km)	Human body (centimeters / meters)
Node Number	Many redundant nodes for wide area coverage	Fewer, limited in space
Node Tasks	Node performs a dedicated task	Node performs multiple tasks

Node Size	Small is preferred, but not important	Small is essential
Network Topology	Very likely to be fixed or static	More variable due to body movement
Node Replacement	Performed easily, nodes even disposable	Replacement of implanted nodes difficult
Power Supply	Accessible and likely to be replaced more easily and frequently	Inaccessible and difficult to replace in an implantable setting
Energy Scavenging	Most likely solar and wind power	Most likely motion (vibration) and thermal (body heat)
Biocompatibility	Not a consideration in most applications	A must for implants and some external sensors
Security Level	Lower	Higher, to protect patient information
Wireless Technology	Bluetooth, ZigBee, GPRS, WLAN, .	Low power technology required e.g. Bluetooth 4.0

To build any wireless device, the first essential step is to study the transmission channel and model it accurately. In order to develop a general and accurate BAN channel model, it is important to study the propagation mechanism of wireless radio waves on and inside the body. Such a study will reveal the underlying propagation characteristics. This will assist in the development of enhanced BAN transceivers, which are better suited to the body environment. The human body is a very complex environment and has not been studied explicitly for wireless communication.

1.2 Motivation For the Research

Measurement and modeling of radio propagation for high speed wireless communications and localization is a challenging field of science and engineering. This is due to the fact that the radio channel suffers from temporal, spatial and frequency selective fading caused by very complex random variations of the multipath components carrying a radio signal from one location to another.

The human body channel suffers from severe multipath propagation and heavy shadow fading conditions so that measurements for localization are far from accurate in many instances. Previous literature on BANs such as [8] have mostly concentrated on narrowband measurements and simulations for RSS for communication applications. RSS-based techniques can also be used for localization applications. Recent developments in wireless communications have resulted in the design of low-cost, low-power, multi-functional, small-sized sensor nodes that can communicate over short distances. One of the major applications in BAN using these sensor nodes is wireless capsule endoscopy. Although this technology has reached an acceptable level as far as image transmission is concerned, it still has limitations with respect to accurate localization of the capsule inside the body. The need for accurate location information for this application has attracted considerable interest. There are many factors that affect the choice of the localization algorithm to be used for a specific application. Some of these factors are the network architecture; the node density; the geometrical shape of the network area and the distribution of the sensors in that area; sensor time synchronization and the signaling bandwidth. The performance of the chosen algorithm can be expressed in terms of accuracy, precision, complexity, scalability, robustness and cost. RSS measurements are relatively inexpensive, simple to implement in hardware, and less sensitive to bandwidth limitations and harsh

propagation environment. They are important and popular topics for localization research. Yet, RSS measurements are notoriously unpredictable; hence there was a need to explore the possibility of using TOA ranging techniques for the human body channel. Unlike RSS based localization, which can be implemented using the RSS based human body channel model [9], there is lack of a TOA channel model that is widely accepted for precisely predicting the time of arrival of the transmitted signal for localization purpose. Hence we need to resort to some computational techniques such as FDTD to find the time of flight of the signal for localization purpose. The behavior of a TOA sensor in human body multipath propagation is highly sensitive to the bandwidth of the sensor. We refer to the distance error caused by erroneous estimate of the TOA as the *distance measurement error*. For a given multipath condition we expect that as we increase the bandwidth the distance measurement error becomes smaller. [10]

1.3 Contribution of the Thesis

At this stage it is worthwhile to look at the contribution which this thesis makes: In the first part of the thesis, we analytically derive the Bayesian Cramér–Rao lower bound on localization accuracy in 3D. The equations are simplified to a point where they can be applied to find bounds for any arbitrary sensor configuration. We then use these equations to find the bounds for localization of a wireless endoscopy capsule inside the human body using the implant-to-surface path loss model. In the second part of the thesis, we resort to the computational technique, FDTD for simulation of TOA based localization due to lack of availability of TOA based model. We highlight the potential drawbacks of the FDTD simulation method, and present a novel perspective on FDTD simulation which led to overcome at least one of these drawbacks. We

then use this method, for comparing narrowband and wideband simulation inside the homogeneous human body.

1.4 Summary of Thesis Chapters

This Thesis is organized into five chapters. Chapter 2 provides a more detailed discussion of Body Area Networks. Some of the most popular localization techniques are discussed there and the chapter concludes with highlighting the challenges in localization in the context of BAN. Chapter 3 introduces the RSS based localization scheme, and derives the localization bounds that can be achieved for the wireless capsule endoscopy application considering the randomness in the transmitted power. In Chapter 4, we resort to TOA based localization for in-body localization using, FDTD simulation technique. Chapter 5 presents the conclusions of this research and outlines future research.

Chapter 2

Body Area Network and localization

Wireless Body Area Network (WBAN) is a wireless technology worn by a human being, creating personal network around the person's body for the purpose of monitoring or treating them as a patient. The WBAN consist of miniaturized, low power and noninvasive or invasive wireless biosensors, seamlessly placed on or implanted in the human body in order to provide an adaptable and smart healthcare system. Each tiny biosensor is capable of performing its own task as well as communicating with a network coordinator or Personnel Digital Assistant (PDA). The network coordinator sends the patient's information to a remote server for diagnosis and prescription.

Started as a Study Group in 2006 and motivated by the increasing research and industry interest in WBANs, the IEEE Standards Association decided to form the IEEE 802.15 Task Group 6 in November 2007. It describes itself as follows: *“The IEEE 802.15 Task Group 6 (BAN) is developing a communication standard optimized for low power devices and operation on, in or*

around the human body (but not limited to humans) to serve a variety of applications including medical, consumer electronics / personal entertainment and other” [11].

2.1 Localization

Localization is defined to be the process of accurately pin-pointing the position of an electronic object in a given area. Since conventional methods used in outdoor positioning cannot be used for accurate indoor geo-location or localization within the human body, they are treated as separate areas of interest.

The need for more accurate and pervasive localization technology has been the driving force behind development of location aware applications and systems. The social, mobile and healthcare applications also tend to favor the use of these technologies, due to their precise and sometimes vital requirements. Without using these technologies some of the social and healthcare networking applications will not meet expectations. Due to recent advancements, we have an established base of localization techniques, but most of them have been designed with a view towards the requirements of particular applications.

2.2 Localization techniques:

Sensor network localization algorithms estimate the locations of sensors with initially unknown location information by using knowledge of the absolute positions of a few sensors and inter-sensor measurements such as distance and bearing measurements. Sensors with known location information are called *anchors* and their locations can be obtained by installing anchors at points with known coordinates.

2.2.1 Distance estimation via received signal strength measurements

The first category of distance related measurement techniques estimates the distances between neighboring sensors from the received signal strength measurements [12]-[16]. These techniques are based on a standard feature found in most wireless devices, a received signal strength indicator (RSSI). They are attractive because they require no additional hardware, and are unlikely to significantly impact local power consumption, sensor size and thus cost. In free space, other things being equal the RSS varies as the inverse square of the distance d between the transmitter and the receiver. Let us denote this received power by $P_r(d)$. The received power $P_r(d)$ is related to the distance d through the Friis equation [17]:

$$P_r(d) = \frac{P_t G_t G_r \lambda^2}{(4\pi)^2 d^2} \quad (2.1)$$

Where P_t is the transmitted power, G_t is the transmitter antenna gain, G_r is the received power gain and λ is the wavelength of the transmitted signal.

The free-space model however is an over-idealization, and the propagation of a signal is affected by reflection, diffraction and scattering. Of course, these effects are environment (indoors, outdoors, rain, buildings, etc.) dependent. However, it is accepted on the basis of empirical evidence that it is reasonable to model the RSS $P_r(d)$ at any value of d at a particular location as a random and log-normally distributed random variable with a distance-dependent mean value [18], [19]

$$P_r(d)[dBm] = P_0(d)[dBm] - 10\alpha \log_{10} \left(\frac{d}{d_0} \right) + S \quad (2.2)$$

where $P_0(d)[dBm]$ is a known reference power value in dB above a milliwatt at a reference distance d_0 from the transmitter; α is the path loss exponent that measures the rate at which the RSS decreases with distance and the value of α depends on the specific propagation environment; S is a zero mean Gaussian distributed random variable with standard deviation σ and it accounts for the random effect of shadowing [17].

It is trivial to conclude that, given the RSS measurement, P_{ij} , between a transmitter i and a receiver j , a maximum likelihood estimate of the distance d_{ij} between the transmitter and the receiver is:

$$\hat{d}_{ij} = d_0 \left(\frac{P_{ij}}{P_0(d_0)} \right)^{-1/n_p} \quad (2.3)$$

Note that P_{ij} and $P_0(d_0)$ in the above equation are measured in milliwatts instead of dB milliwatts. The estimated distance \hat{d}_{ij} can be related to the true distance:

$$\hat{d}_{ij} = d_{ij} 10^{-\frac{S}{10\alpha}} \quad (2.4)$$

Thus the maximum likelihood estimate in the above equation is a biased estimate of the true distance and an unbiased estimate is given by:

$$\hat{d}_{ij} = d_0 \left(\frac{P_{ij}}{P_0(d_0)} \right)^{-1/n_p} e^{-\frac{\sigma^2}{2\eta^2\alpha^2}} \text{ where } \eta = \frac{10}{\ln(10)} \quad (2.5)$$

2.2.2 Round-trip propagation time measurements:

One-way propagation time and round-trip propagation time measurements are also generally known as time-of-arrival measurements. Distances between neighboring sensors can be estimated from these propagation time measurements. One-way propagation time measurements

measure the difference between the sending time of a signal at the transmitter and the receiving time of the signal at the receiver. It requires the local time at the transmitter and the local time at the receiver to be accurately synchronized. This requirement may add to the cost of sensors by demanding a highly accurate clock and/or increase the complexity of the sensor network by demanding a sophisticated synchronization mechanism. This disadvantage makes one-way propagation time measurements a less attractive option than measuring round-trip time in WSNs. Round-trip propagation time measurements measure the difference between the time when a signal is sent by a sensor and the time when the signal returned by a second sensor is received at the original sensor. Since the same clock is used to compute the round-trip propagation time, there is no synchronization problem. The major error source in round-trip propagation time measurements is the delay required for handling the signal in the second sensor. This internal delay is either known via *a priori* calibration, or measured and sent to the first sensor to be subtracted. Time delay measurement is a relatively mature field. The most widely used method for obtaining time delay measurement is the generalized cross-correlation method [20], [21].

A recent trend in propagation time measurements is the use of ultra wide band (UWB) signals for accurate distance estimation [22], [23]. A UWB signal is a signal whose bandwidth to center frequency ratio is larger than 0.2 or a signal with a total bandwidth of more than 500 MHz. UWB can achieve higher accuracy because its bandwidth is very large and therefore its pulse has a very short duration. This feature makes fine time resolution of UWB signals and easy separation of multipath signals possible.

2.2.3 Time-difference-of-arrival (TDOA) measurements

There is a category of localization algorithms utilizing TDOA measurements of the transmitter's signal at a number of receivers with known location information to estimate the location of the transmitter. Figure 3 below shows a TDOA localization scenario with a group of four receivers at locations r_1, r_2, r_3, r_4 and a transmitter at r_t .

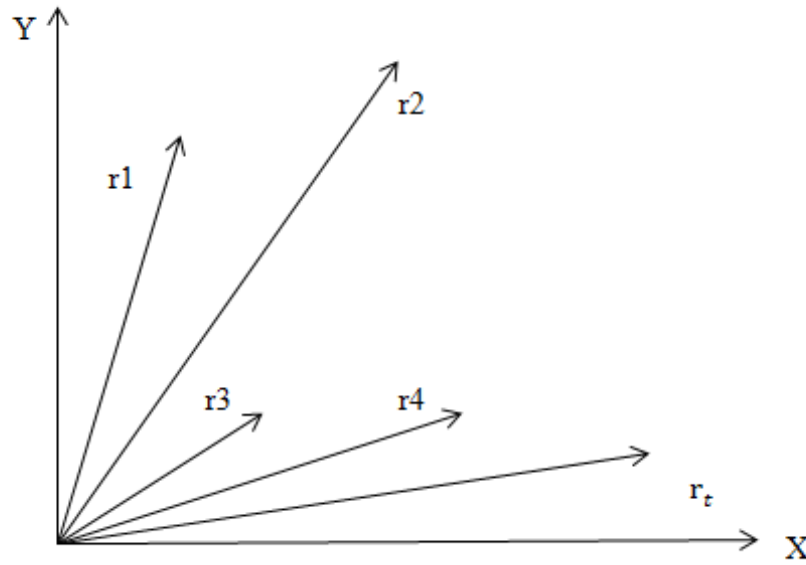


Figure 3: Localization using time-difference-of-arrival measurements

The TDOA between a pair of receivers i and j is given by

$$\Delta t_{ij} \triangleq t_i - t_j = \frac{1}{c(\|r_i - r_t\| - \|r_j - r_t\|)}, \quad i \neq j \quad (2.6)$$

Where t_i and t_j are the time when a signal is received at receivers i and j respectively, c is the propagation speed of the signal, and $\|\cdot\|$ denotes the Euclidean norm. Measuring the TDOA of a signal at two receivers at separate locations is a relatively mature field [24]. The most widely

used method is the generalized cross-correlation method, where the cross-correlation function between two signals s_i and s_j received at receivers i and j is given by integrating the product of two received signals for a sufficiently long time period T :

$$\rho_{i,j}(\tau) = 1/T \int_0^T s_i(t)s_j(t - \tau)dt \quad (2.7)$$

The cross-correlation function can also be obtained from an inverse Fourier transform of the estimated frequency domain cross-spectral density function. Frequency domain processing is often preferred because the signals can be filtered prior to computation of the cross-correlation function. The cross correlation approach requires very accurate synchronization among receivers but does not impose any requirement on the signal transmitted by the transmitter. The accuracy and temporal resolution capabilities of TDOA measurements will improve when the separation between receivers increases because this increases differences between times-of-arrival [25].

Yet another factor affecting the accuracy of TDOA measurement is multipath. Overlapping cross-correlation peaks due to multipath often cannot be resolved. Even if distinct peaks can be resolved, a method must be designed for selecting the correct peak value, such as choosing the largest or the first peak [26].

2.3 Challenges in Localization

Channel measurement and modeling for inside the human body to support waveform transmission for RF localization is in its infancy. From an innovative research point of view, measurement and modeling of radio propagation inside and around the human body offers unique challenges making this area very appealing for basic research. These challenges are raised by several specifics of the human body medium and its applications that are profoundly different from the traditional indoor radio propagation challenges.

In RSS based localization, wireless sensors communicate with neighboring sensors, so that the RSS of Radio Frequency (RF) signals can be measured by each receiver during normal data communication without presenting additional bandwidth or energy requirements. RSS measurements are relatively inexpensive, simple to implement in hardware, less sensitive to bandwidth limitations and harsh propagation environment. They are important and popular topics for localization research. Yet, RSS measurements are notoriously unpredictable. If they are to be useful parts of a robust localization system, their sources of error must be well understood.

2.3.1 Non-Homogeneity:

The important difference between propagation inside human body and the overall indoor propagation is that the medium for propagation inside the body is close to liquids, which have substantially different conductivity than the air which is the main medium for the indoor radio propagation. In addition, the interior of the human body offers a non-homogeneous environment with non-geometric boundaries for radio propagation, while indoor is a non-homogeneous environment with fairly geometric boundaries for radio propagation. Inside a typical indoor environment most of the propagation time is spent through the air and the second important medium are the walls that have geometric shapes.

These features allow us to construct a simpler radio propagation mechanism such as ray-tracing to describe the radio propagation in indoor environment using ray optics methods [27]. The interior of the human body is a non-geometric and nonhomogeneous medium for radio propagation that will not allow application of simple ray tracing techniques. Conductivity of the different organs, bones and the muscle tissues are also widely different posing a challenge for the

analysis of time of flight for the signal that is commonly used for ranging using TOA of the received signal.

The indoor environment is a very complex propagation medium for localization as well [28], but we can easily measure the wideband radio channel characteristics using a network analyzer and develop empirical statistical models for the TOA [29]. In radio propagation analysis inside the human body we cannot simply place antennas inside to collect empirical data for statistical radio propagation modeling. In indoor areas we use the time of flight of the signal to measure the distance between the transmitter and the receiver by multiplying the time of flight with the speed of radio wave propagation in the air that is the same as speed of light. Since the human body is a non-uniform liquid medium the speed of radio wave propagation is different from the speed in the free space and it also differs in various organs.

The most accurate ranging technique for localization used in popular applications such as GPS is TOA ranging. In traditional TOA localization applications the time of flight of a transmitted pulse with a sharp peak is measured at the receiver and distance is estimated by multiplying the time of flight with the velocity of propagation that is the same as velocity of light. This works because radio wave propagates in the air, which is a homogeneous environment with a uniform permittivity. The human body is a non-homogeneous medium and permittivity values in different organs are different and that causes a new source of ranging error. The ranging error is often caused by bandwidth limitation and SNR limitation. Propagation velocity inside human body is expressed as a function of the relative permittivity:

$$v(\omega) = \frac{c}{\sqrt{\epsilon_r(\omega)}} \quad (2.8)$$

Where velocity is a function of permittivity and the permittivity is a function of the frequency of operation. On the other hand, the human body is formed by various organs with

complex structures. Each organ has different characteristics of conductivity and relative permittivity. Inside the human body, the received signal is also distorted through the multipath channel caused by the refraction at the boundaries between different tissues. Therefore, TOA ranging inside the human body is very challenging.

2.3.2 Movement of the Body:

Effects of human body motion on RF propagation in and around the human body is a very important topic; because usually sensors are mounted on the torso, hands and feet, while a body mounted relay with larger size is mounted on the hips using a belt. In most popular envisioned applications for BANs the relay is used for communication to external access points connecting the network to the backbone Internet. The speed of motion of the sensors with respect to the relay and the external access point is quite different.

As far as the strength of the received signal is concerned, the movement of the body has a significant effect [30]. In [31] it is shown that arm motions to the front and side of the body can have a small impact on the received power. More significant variations are found when the arms are moved so that they block the line of sight between the two antennas. In [32] a preliminary system model for gait analysis has been proposed. It is concluded that significant attenuation can occur (up to 20 dB) when a body limb is moved in between the TX and Rx antennas. According to [33] the movement of the limbs can induce an attenuation of 30 dB or more. A similar conclusion was found in an actual implementation [34] where the sensors communicate directly with the personal device using an RF-radio operating at 868 MHz, loss rates of more than 50% were found when the body was in motion.

2.4 Antenna Effect

An antenna placed on the surface or inside a body will be heavily influenced by its surroundings. The consequent changes in antenna pattern and other characteristics need to be understood and accounted for during any propagation measurement campaign. The form factor of an antenna will be highly dependent on the requirements of the application. For Medical Implant Communication Service (MICS) applications, for example, a circular antenna may be suitable for a pacemaker implant, while a helix antenna may be required for a stent or urinary implant. The form factor will affect the performance of the antenna and, the antenna performance will be very important to the overall system performance. Therefore, an antenna which has been designed with respect to the body tissues (or considering the effect of human body) shall be used for the channel model measurements.

The BAN antennas may be classified into two main groups:

- **Electrical antennas, such as dipole:** An electrical antenna typically generates large components of E-field normal to the tissue interface, which overheat the fat tissue. This is because boundary conditions require the normal E-field at the interface to be discontinuous by the ratio of the permittivity, and since fat has a lower permittivity than muscle, the E-field in the fat tissue is higher.
- **Magnetic antennas, such as loop:** A magnetic antenna produces an E-field mostly tangential to the tissue interface, which seem not to couple as strongly to the body as electrical antennas. Therefore, it does not overheat the fat. There are antennas same as helical-coil, which is similar to a magnetic antenna in some respect, but its heating characteristics appear to be more like an electrical antenna. The strong E-field generated between the turns of coil is mainly responsible for tissue heating.

It should be noted that the specific absorption rate (SAR) in the near field of the transmitting antenna depends mainly on the H-field; however, SAR in the far field of the transmitting antenna depends mainly on the E-field.

2.5 Electrical Properties of Body Tissues

The electrical properties of human tissues (relative permittivity ϵ_r and conductivity σ_{eff}) control the propagation, reflection, attenuation, and other behavior of electromagnetic fields in the body. These properties depend strongly on the tissue type and the frequency of interest. Temperature, blood or fluid perfusion, and individual differences are second-order effects that are normally not considered. The body is so weakly magnetic that generally μ_r is assumed to be 1, except for magnetic resonance imaging and spectroscopy applications where a very large magnetic field is used.

Table II shows the electrical properties of several different tissues in the body at 433 MHz, which is a commonly used frequency for Industrial Scientific Medical (ISM) applications. A common approximation is that the body can be modeled using average properties of 2/3 muscle, which means that both ϵ_r and σ at the frequency of interest are multiplied by 2/3. This is suitable for addressing global questions such as total power absorbed in the body, but is generally not suitable for evaluating near-field effects such as peak SAR.

The electrical properties of the body (ϵ_r and σ_{eff}) control the wavelength and attenuation. The attenuation of the field is calculated as $e^{-\alpha z}$, where z is the distance the wave must propagate through that tissue. At 433 MHz, 69% of the field is transferred through 10 cm of fat, and 11% is transferred through 10 cm of muscle. The higher-water-content (higher-conductivity) tissues have more attenuation. The wavelength is calculated from $2\pi/\beta$ (meters).

The wavelength at 433 MHz in fat is 30 cm, and in muscle is 8 cm. A typical rule of thumb is that an antenna should be half a wavelength, which would be 4 cm in muscle. While this still seems too large for most implantable devices, specialized antenna designs can achieve performance in the body at this frequency.

Electromagnetic measurements such as assessment of cellular telephones, evaluation of the performance of telemetry (communication) devices implanted in the body, or other measurement applications often require body-simulant materials. These can be solid, semisolid, or (most commonly) liquid materials that have electrical properties that mimic those of human tissues.

Table II: Electrical Properties of Different Tissues in Human Body

Tissue	ϵ^r	σ_{eff}	Tissue	ϵ^r	σ_{eff}
Air (vacuum)	1	0	Heart	60.74	0.9866
Blood	57.3	1.72	Kidney	57.3	1.152
Breast fat	5.62	0.04953	Liver	50.34	0.68
Cerebellum	52.9	0.91	Lung deflated	52.83	0.7147
Fat	5.028	.04502	Muscle	64.2	0.9695
Skin (dry)	42.48	0.5495	Small intestine	74.1	2.053
Stomach	74.55	1.120	Nerve	35.7	0.500

Chapter 3

Performance Bounds for Wireless Capsule Endoscopy with random transmit power

3.1 Wireless Capsule Endoscopy

Endoscopy is a medical procedure for examining the gastro-intestinal (GI) track of the human body to find the possibility of tumor or disease or bleeding. The orthodox endoscopy process uses a tube like instrument called an endoscope. The endoscope is put into the body to look inside, and perform certain surgical procedures. The average adult digestive track is approximately 30 feet in length [39][42]. The top 4 feet (Upper GI) includes the esophagus (food pipe) and stomach and first portion of the small intestine, called the duodenum. The bottom 6 feet makes up the colon and rectum. In between, lies the rest of the 20 feet of small Intestine where the process of digestion actually occurs [42]

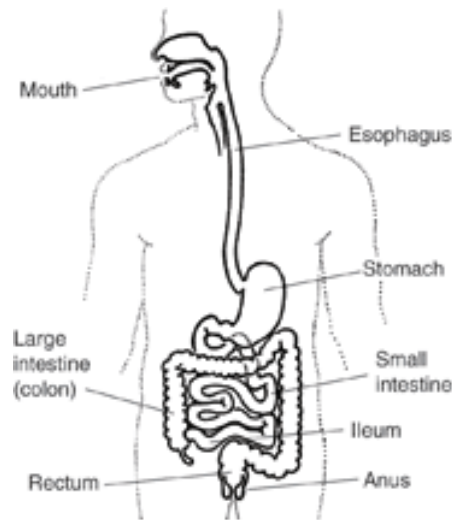


Figure 4: The human Gastro-Intestinal Track

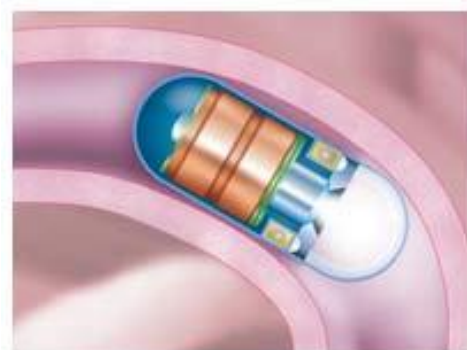
The traditional endoscopy involves gastroscopy which is used to check the first 4 feet of the upper digestive track and colonoscopy to evaluate the colon and rectum. Thus, most of the 20 feet of small intestine (colored green above) lies beyond the reach of these two procedures. Fortunately, most bleeding problems seem to occur in the area than can be "scoped" and the source of bleeding is usually found and treated [41]. Common problems would include hiatal hernia, gastritis, ulcers, polyps, and, sometimes, stomach or colon cancer. But it is not uncommon for doctors to evaluate a patient with unexplained anemia and neither gastroscopy nor colonoscopy scope examinations reveal the diagnosis. By a process of elimination, it then becomes likely that the source of bleeding lies somewhere in-between - below the reach of the Gastroscope and above the reach of the Colonoscope - in the 20 feet of small intestine. How then is this area examined? Thus, a direct view of the small intestine has remained elusive. Attempts have been made to develop longer endoscopic instruments. This technique called push enteroscopy has had only limited success [41]. The longer instruments are difficult to control and

manipulate and are hard to maintain. The accuracy of push enteroscopy is still limited since even in the best of hands the entire small intestine is not visualized.

In 1981, an Israeli physician, Dr. Gavriel Iddan, began development of a video camera that would fit inside a pill [41]. Technology was not ready and the idea was put on hold. It took 20 years for technology to catch up with Dr. Iddan. In 2001, the FDA approved the Given Diagnostic Imaging System [43]. This may sound like science fiction, but this 11 x 26 mm capsule weighs only 4 gms (about 1/7th of an ounce) and contains a color video camera and wireless radiofrequency transmitter, 4 LED lights, and enough battery power to take 50,000 color images during an 8-hour journey through the digestive track. About the size of a large vitamin, the capsule is made of specially sealed biocompatible material that is resistant to stomach acid and powerful digestive enzymes [41]. Another name for this new technique is *Wireless Capsule Endoscopy*.



(a)



(b)

Figure 5: a) The wireless endoscopy capsule b) The capsule moving through GI track

Wireless capsule endoscopy has emerged as a new technology for detecting diseases inside the GI track without causing much pain to the patient under observation; hence, it has been used widely in hospitals to check the status of the GI track.

Patients report that the video capsule is easier to swallow than an aspirin. It seems that the most important factor in ease of swallowing is the lack of friction [43]. The capsule is very smooth, enabling it to slip down the throat with just a sip of water. After the Given M2A capsule is swallowed, it moves through the digestive track naturally with the aid of the peristaltic activity of the intestinal muscles. The patient comfortably continues with regular activities throughout the examination without feeling sensations resulting from the capsule's passage. During the 8 hour exam, the images are continuously transmitted to special antenna pads placed on the body and captured on a recording device about the size of a portable Walkman which is worn about the patient's waist. After the exam, the patient returns to the doctor's office and the recording device is removed. The stored images are transferred to a computer PC workstation where they are transformed into a digital movie which the doctor can later examine on the computer monitor. Patients are not required to retrieve and return the video capsule to the physician. It is disposable and expelled normally and effortlessly with the next bowel movement.

3.2 Localization in Wireless Capsule Endoscopy

A significant issue for capsule endoscopy tele-operated procedures is to know where the device is positioned during GI track examination. During the examination process, if the doctor examines the tumor, disease or bleeding in a particular image, it is important to really map the picture accurately to the location of the capsule when that picture was taken by the capsule to

determine precise location of the defect. This is the area of the wireless capsule endoscopy technology which is lacking in terms of accurately finding the location of the capsule and hence the tumors. After the examination by WCE, the physician may want to revisit the sites of interest for further diagnosis or treatment. Accurate location information of the capsule can help in both reducing the time needed for assessing the photos and assisting the physicians for follow-up interventions.

Various technologies for localization of the capsule have been explored in feasibility studies. The original idea is to use a spatially scanning system to locate the points with the strongest RSS. The system is non-commercial and cumbersome. Frisch et al [45] developed an RF triangulation system using an external sensor array that measures signal strength of capsule transmissions at multiple points and uses this information to estimate the distance. The average experimental error is reported to be 37.7mm [46]. Other techniques include ultrasound [47], time of arrival (TOA) based pattern recognition [48], magnetic tracking [49], [50] and computer vision [51], [52]. Among these technologies, RF signal based localization systems have the advantage of application-non-specific and relatively low cost for implementation. Therefore, it has been chosen for use with the Smart-pill capsule [53] in USA and the M2A capsule [54] in Israel. Generally, the RF localization technique is based on TOA, angle of arrival (AOA) or RSS measurements. A widely known benefit of TOA based techniques is their high accuracy relative to RSS and AOA based techniques. However, the strong absorption of human tissue causes large errors in TOA estimation and the limited bandwidth (402-405MHz) of the MICS band prevent us from high resolution TOA estimation. The problem is made even worse by the GI movement, and the filling and emptying cycle, resulting in unpredictable ranging error [55].

In this thesis, we will address the issues related to the RSS triangulation technique. The RSS Triangulation technique is based on the path loss model from implant tissues to body surface. The model is used to calculate the distance between each external sensor and the capsule, then at least 4 link distances are used to calculate the location of the capsule in 3D space. Currently, most of the researchers have focused on developing the algorithms and mathematical models for solving the triangulation problem [56]. Here, we take a different approach. Based on the statistical implant path loss model developed in [57], we focus on the accuracy possible for capsules in the GI tract using RSS based triangulation technique. The CRB presented in this quantify the limits of localization accuracy with certain reference-points topology, implant path loss model. Our aim is to analyze the accuracy achievable at various organs when there is randomness in transmit power and determine if the accuracies are enough for endoscopy applications. Similar work has been done for indoor geolocation applications [59] and robot localization applications [60].

3.3 Randomness in Transmit Power

In realistic sensor networks, the sensors are not designed to know their precise transmitted power level due to cost of the device calibration. Although, they may report that the transmitted power is at a particular level; the actual power transmitted varies by a few dB about this nominal value [61]. The major factors that causes transmitted power variance for body area networks are as follows: a) Device manufacturing variation and battery level variation from sensor to sensor, b) Movement of the human body due to locomotion and changes in the orientations of the antennas, c) The sensors antennas might not be at the same distance from the human body surface at a

given time. Some antennas might be touching the body while others might be few mm's away from the body.

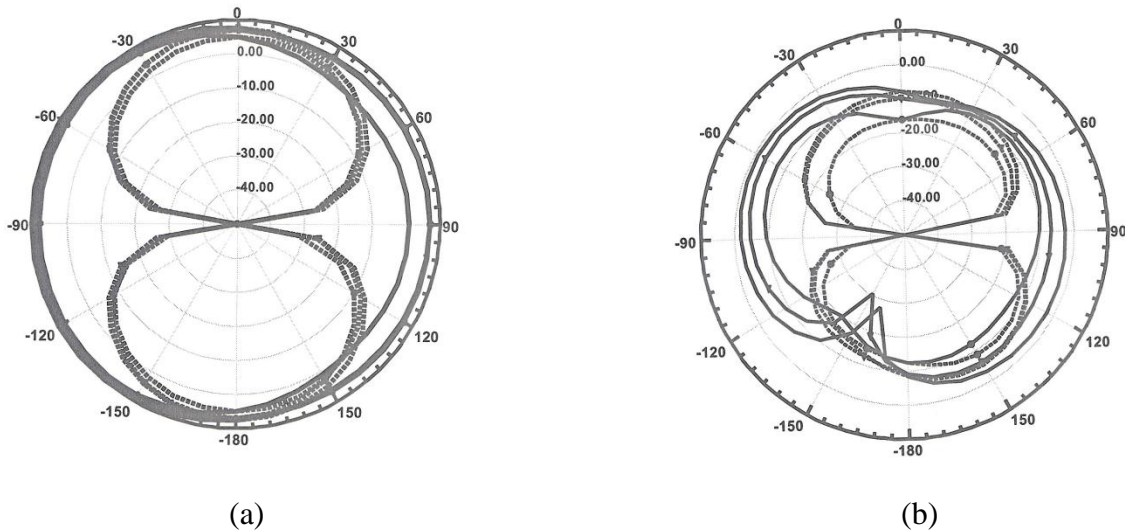


Figure 6: Plot showing the decrease in the gain of the antenna when the antenna is placed on the surface of the body [62]. a) Gain of antenna 15mm away from body, b) gain of antenna touching the body

As reported in [62], and shown in the Figure 6, antenna touching the body has a lower gain (plot of gain on the right) than the antenna 15mm away from the body (Plot of gain on the left). All these factors contribute to the randomness in the transmitted power which affects the localization accuracy.

3.4 Channel model for Body Area network

A channel model is useful in determining the mechanisms by which propagation in the particular environment occurs, which in turn are useful in the development of a communication system. By examining the details of how a signal is propagated from the transmitter to the receiver for a number of experimental locations, a generic model may be developed that highlights the

important characteristics of a given propagation environment. Generic models of indoor communications can then be applied to specific situations to describe the operation of a radio system, and may also be used to generate designs that are particularly well-disposed to supporting radio communication systems.

The term channel refers to the medium between the transmitting antenna and the receiving antenna. The characteristics of wireless signal changes as it travels from the transmitter antenna to the receiver antenna. These characteristics depend upon the distance between the two antennas, the path(s) taken by the signal, and the environment (buildings and other objects) around the path. The profile of received signal can be obtained from that of the transmitted signal if we have a model of the medium between the two. This model of the medium is called channel model. In general, the power profile of the received signal can be obtained by *convolving* the power profile of the transmitted signal with the impulse response of the channel. Convolution in time domain is equivalent to multiplication in the frequency domain. Therefore, the transmitted signal x , after propagation through the channel H becomes y :

$$Y(f) = H(f)X(f) + n(f) \quad (3.1)$$

Here $H(f)$ is channel response, and $n(f)$ is the noise. The three key components of the channel response are path loss, shadowing, and multipath.

The channel model is not simple for a BAN (body area network) because of the complexity of the human tissue structure and body shape. If the signal propagates in free space, the path loss model in dB between the transmitter and the receiver is related only to the distance d , and this relationship is given by

$$PL(d) = PL_0 + 10\alpha \log_{10}(d/d_0) \quad (3.2)$$

Where PL_0 is the path loss at a reference distance d_0 . The parameter α , is the path loss exponent value, indicating the rate at which the path loss increases as distance d increases

To take into account the shadowing effect which is caused by variation in the environment around the human body and also the movement of the body parts which eventually affects the received signal strength, we add an additional term S to the above equation. The resulting final equation is given as

$$PL(d) = PL_0 + 10\alpha \log_{10}(d/d_0) + S \quad (3.3)$$

Thus, here S is the random variable in dB around the mean and represents the shadow fading phenomenon.

The statistical path loss model for medical implant communication was developed by the National Institute of Science and Technology (NIST) at the MICS band [57]. The parameters of implant to body surface path loss model are summarized in Table III, where σ_{dB} is the standard deviation of the shadow fading S .

Table III: Parameters for the Statistical Implant to Body Surface Path Loss Model ($d_0 = 50\text{mm}$)

[57]

Implant to body surface	PL_0 (dB)	α	σ_{dB}
Deep Tissue	47.14	4.26	7.85
Near Surface	49.81	4.22	6.81

3.5 Derivation of the Bayesian Cramér–Rao bound

In this Section, we derive the 3D CRB based on the path loss model discussed in Section 3.4 (i.e., Channel model for Body Area network). The Bayesian CRB for randomness in power, has already been derived in two dimensions [61], here we derive the bounds in three dimensions by extending the results obtained in two dimensions [63]. The unknown parameters to be estimated are the x, y, and z coordinates of the capsules. We denote these unknown parameters by a vector

$$\begin{aligned}
 \theta &= [x^T, y^T, z^T, \Pi^T]^T \\
 x &= [x_1, \dots, x_N]^T \\
 y &= [y_1, \dots, y_N]^T \\
 z &= [z_1, \dots, z_N]^T \\
 \Pi &= [\Pi_{01}, \dots, \Pi_{0N}]^T
 \end{aligned} \tag{3.4}$$

There are $3n + N$ parameters since none of the N sensors have perfect knowledge of their transmit power and n capsules have no perfect knowledge of their coordinates. We assume that all the sensors from $n + 1$ to N have perfect knowledge of their coordinates. The Bayesian CRB [64], also called the Van trees inequality, states that any estimator $\hat{\theta}$ must have error

Correlation matrix R_ϵ satisfying

$$R_\epsilon \geq F^{-1} \Delta [F_\theta + F_p]^{-1} \tag{3.5}$$

Where $R_\epsilon \Delta E[(\hat{\theta} - \theta)(\hat{\theta} - \theta)^T]$

With F_θ and F_p are the Fisher information matrix and prior information matrix respectively and are given by the following equations

$$F_{\theta} = -E[\nabla_{\theta}(\nabla_{\theta} \ln f(\{p_{ij}\}_{ij} | \theta))^T] \quad (3.6)$$

$$F_p = -E[\nabla_{\theta}(\nabla_{\theta} \ln f(\theta))^T] \quad (3.7)$$

Where p_{ij} is the bidirectional measurement vector. The a priori information matrix is given below

$$F_p = \text{diag}\{[0_n^T, 0_n^T, 0_n^T, 1_n^T/\sigma_n^2]\} \quad (3.8)$$

Where 0_n is a n-length vector of zeros and 1_n is N length vectors of ones and σ_n^2 is the variance of the random variable Π_{0i} (the power at 50 mm (d_0) distance from transmitter i) which is assumed to have an i.i.d. Gaussian prior distribution for every sensor i.

As shown in [61], we model the bi-directional measurements P_{ij} and P_{ji} using vector $p_{ij} = [P_{ij}; P_{ji}]$ as a bi-variate Gaussian with mean μ_{ij} and variance C_{ij} , where

$$\mu_{ij} = \begin{bmatrix} \Pi_{0j} - 10\alpha \log_{10} \frac{\|r_i - r_j\|^2}{d_0^2} \\ \Pi_{0i} - 10\alpha \log_{10} \frac{\|r_i - r_j\|^2}{d_0^2} \end{bmatrix} \quad (3.9)$$

$$C_{ij} = \sigma_{dB}^2 \begin{bmatrix} 1 & \rho \\ \rho & 1 \end{bmatrix} \quad (3.10)$$

Where α is the path loss exponent of the environment of interest, and ρ is the correlation coefficient, $0 < \rho < 1$.

Before calculating the Fisher information matrix, we transform the two directional measurements p_{ij} for the purposes of discussion. It can be seen both intuitively and from equation 3.9 and 3.10

that a full-rank transformation of the measurements does not change their Fisher information matrix. We choose to transform each pair of measurements p_{ij} by orthogonal matrix A ,

$$\tilde{p}_{i,j} = Ap_{ij}, \quad A = 1/2 \begin{bmatrix} 1 & 1 \\ 1 & -1 \end{bmatrix} \quad (3.11)$$

For notational purposes, we denote $\tilde{p}_{i,j} = [\bar{p}_{ij}, p_{ij}^\Delta]$. The top element of $\tilde{p}_{i,j}$ is the average of the two measurements P_{ij}, P_{ji} , and the bottom element p_{ij}^Δ is half of their difference. These two random variables are still Gaussian, but they are independent, since

$$\tilde{R}_{ij} = A^T C_{ij} A = \sigma_{dB}^2/2 \begin{bmatrix} 1 + \rho & 0 \\ 0 & 1 - \rho \end{bmatrix} \quad (3.12)$$

Thus $\bar{p}_{ij}, p_{ij}^\Delta$ have means $\bar{\mu}_{ij}, \mu_{ij}^\Delta$ respectively, where they are given by

$$\bar{\mu}_{ij} = \frac{\Pi_{0j} + \Pi_{0i}}{2} - 10\alpha \log_{10} \frac{\|r_i - r_j\|^2}{d_0^2} \quad (3.13)$$

$$\mu_{ij}^\Delta = 1/2(\Pi_{0j} - \Pi_{0i}) \quad (3.14)$$

We define $\bar{\mu}$ and μ^Δ as

$$\bar{\mu} = [\bar{\mu}_{i_1 j_1}, \dots, \bar{\mu}_{i_S j_S}]^T \quad (3.15)$$

$$\mu^\Delta = [\mu_{i_1 j_1}^\Delta, \dots, \mu_{i_S j_S}^\Delta]^T \quad (3.16)$$

Where $i_1 j_1, \dots, i_S j_S$ a listing of each unique pair which makes measurement and S is the number of unique pairs measured.

3.5.1 Deriving the fisher information matrix:

As a result of their independence, we split the Fisher information into two matrices, \bar{F}_θ for the average measurements $\{\bar{p}_{ij}\}$, and F_θ^Δ for the difference measurements $\{p_{ij}^\Delta\}$

$$F_\theta = \bar{F}_\theta + F_\theta^\Delta \quad (3.17)$$

We know that for a vector of multivariate Gaussian measurements with mean $\mu(\theta)$ and covariance C (for C not a function of θ), that the Fisher information matrix is given

$$F_\theta = [\nabla_\theta \mu(\theta)]^T C^{-1} [\nabla_\theta \mu(\theta)] \quad (3.18)$$

Thus the two terms are

$$\bar{F}_\theta = [\nabla_\theta \bar{\mu}]^T \bar{C}^{-1} [\nabla_\theta \bar{\mu}] \quad (3.19)$$

$$F_\theta^\Delta = [\nabla_\theta \mu^\Delta]^T (C^\Delta)^{-1} [\nabla_\theta \mu^\Delta] \quad (3.20)$$

Where the respective covariance are

$$\bar{C} = \frac{(1 + \rho)\sigma_{dB}^2}{2} I_{2n+N}, C^\Delta = \frac{(1 - \rho)\sigma_{dB}^2}{2} \quad (3.21)$$

And I_{2n+N} is the $2n+N \times 2n+N$ identity matrix. The elements of $\nabla_\theta \bar{\mu}$ are given as,

$$\frac{\partial \bar{\mu}_{ij}}{\partial x_k} = \begin{cases} -\frac{\alpha_1(x_k - x_j)}{\|z_i - z_j\|^2}, & \text{if } k = i \\ -\frac{\alpha_1(x_k - x_i)}{\|z_i - z_j\|^2}, & \text{if } k = j \\ 0, & \text{otherwise} \end{cases} \quad (3.22)$$

$$\frac{\partial \bar{\mu}_{ij}}{\partial y_k} = \begin{cases} -\frac{\alpha_1(y_k - y_j)}{\|z_i - z_j\|^2}, & \text{if } k = i \\ -\frac{\alpha_1(y_k - y_i)}{\|z_i - z_j\|^2}, & \text{if } k = j \\ 0, & \text{otherwise} \end{cases} \quad (3.23)$$

$$\frac{\partial \bar{\mu}_{ij}}{\partial \Pi_{0k}} = \begin{cases} 1/2, & \text{if } k = i \\ 1/2, & \text{if } k = j \\ 0, & \text{otherwise} \end{cases} \quad (3.24)$$

Where $\alpha_1 = 10\alpha/(\log 10)$. Basically there are six non zero elements of $\nabla_{\theta} \bar{\mu}$ for each pair (i,j)

For $\nabla_{\theta} \mu^{\Delta}$, we have simply that $\frac{\partial \mu_{ij}^{\Delta}}{\partial x_k} = \frac{\partial \mu_{ij}^{\Delta}}{\partial x_k} = 0, \forall i, j, k$, and that

$$\frac{\partial \mu_{ij}^{\Delta}}{\partial \Pi_{0k}} = \begin{cases} -\frac{1}{2}, & \text{if } k = i \\ \frac{1}{2}, & \text{if } k = j \\ 0, & \text{otherwise} \end{cases} \quad (3.25)$$

Using complex algebraic manipulations, we simplify the above equations in matrix form as in

[63]:

$$\begin{aligned} F_{\theta} &= [\nabla_{\theta} \mu(\theta)]^T C^{-1} [\nabla_{\theta} \mu(\theta)] \\ &= \begin{bmatrix} F_{Rxx} & F_{Rxy} & F_{Rxz} & F_{Rx\Pi} \\ F_{Ryx} & F_{Ryy} & F_{Ryz} & F_{Ry\Pi} \\ F_{Rzx} & F_{Rzy} & F_{Rzz} & F_{Rz\Pi} \\ F_{R\Pi x} & F_{R\Pi y} & F_{R\Pi z} & F_{R\Pi\Pi} \end{bmatrix} \end{aligned} \quad (3.26)$$

Thus the decomposed matrices are as follows

$$\begin{aligned} \bar{F}_{\theta} &= [\nabla_{\theta} \bar{\mu}]^T \bar{C}^{-1} [\nabla_{\theta} \bar{\mu}] \\ &= \begin{bmatrix} \bar{F}_{Rxx} & \bar{F}_{Rxy} & \bar{F}_{Rxz} & \bar{F}_{Rx\Pi} \\ \bar{F}_{Ryx} & \bar{F}_{Ryy} & \bar{F}_{Ryz} & \bar{F}_{Ry\Pi} \\ \bar{F}_{Rzx} & \bar{F}_{Rzy} & \bar{F}_{Rzz} & \bar{F}_{Rz\Pi} \\ \bar{F}_{R\Pi x} & \bar{F}_{R\Pi y} & \bar{F}_{R\Pi z} & \bar{F}_{R\Pi\Pi} \end{bmatrix} \end{aligned} \quad (3.27)$$

And

$$F_{\theta}^{\Delta} = [\nabla_{\theta} \mu^{\Delta}]^T (C^{\Delta})^{-1} [\nabla_{\theta} \mu^{\Delta}]$$

$$F_{R\Pi\Pi}^\theta = \begin{bmatrix} F_{Rxx}^\theta & F_{Rxy}^\theta & F_{Rxz}^\theta & F_{Rxx\Pi}^\theta \\ F_{Ryx}^\theta & F_{Ryy}^\theta & F_{Ryz}^\theta & F_{Ry\Pi}^\theta \\ F_{Rzx}^\theta & F_{Rzy}^\theta & F_{Rzz}^\theta & F_{Rz\Pi}^\theta \\ F_{R\Pi x}^\theta & F_{R\Pi y}^\theta & F_{R\Pi z}^\theta & F_{R\Pi\Pi}^\theta \end{bmatrix} \quad (3.28)$$

We now derive the individual elements of the matrix given in above matrices [63]

$$[\bar{F}_{Rxx}]_{k,l} = \begin{cases} b_1 \sum_{i \in H(k)} \frac{(x_k - x_i)^2}{d_{k,l}^4} & k = l \\ -b_1 I_{H(k)}(l) \frac{(x_k - x_i)^2}{d_{k,l}^4} & k \neq l \end{cases} \quad (3.29)$$

$$[\bar{F}_{Ryy}]_{k,l} = \begin{cases} b_1 \sum_{i \in H(k)} \frac{(y_k - y_i)^2}{d_{k,l}^4} & k = l \\ -b_1 I_{H(k)}(l) \frac{(y_k - y_i)^2}{d_{k,l}^4} & k \neq l \end{cases} \quad (3.30)$$

$$[\bar{F}_{Rzz}]_{k,l} = \begin{cases} b_1 \sum_{i \in H(k)} \frac{(z_k - z_i)^2}{d_{k,l}^4} & k = l \\ -b_1 I_{H(k)}(l) \frac{(z_k - z_i)^2}{d_{k,l}^4} & k \neq l \end{cases} \quad (3.31)$$

$$[\bar{F}_{Rxy}]_{k,l} = \begin{cases} b_1 \sum_{i \in H(k)} \frac{(x_k - x_i)(y_k - y_i)}{d_{k,l}^4} & k = l \\ -b_1 I_{H(k)}(l) \frac{(x_k - x_i)(y_k - y_i)}{d_{k,l}^4} & k \neq l \end{cases} \quad (3.32)$$

$$[\bar{F}_{Rxz}]_{k,l} = \begin{cases} b_1 \sum_{i \in H(k)} \frac{(x_k - x_i)(z_k - z_i)}{d_{k,l}^4} & k = l \\ -b_1 I_{H(k)}(l) \frac{(x_k - x_i)(z_k - z_i)}{d_{k,l}^4} & k \neq l \end{cases} \quad (3.33)$$

$$[\bar{F}_{Ryz}]_{k,l} = \begin{cases} b_1 \sum_{i \in H(k)} \frac{(y_k - y_i)(z_k - z_i)}{d_{k,l}^4} & k = l \\ -b_1 I_{H(k)}(l) \frac{(y_k - y_i)(z_k - z_i)}{d_{k,l}^4} & k \neq l \end{cases} \quad (3.34)$$

$$[\bar{F}_{R_x\Pi}]_{k,l} = \begin{cases} b_2 \sum_{i \in H(k)} \frac{(x_k - x_i)}{2d_{k,l}^2} & k = l \\ -b_2 I_{H(k)}(l) \frac{(x_k - x_i)}{2d_{k,l}^2} & k \neq l \end{cases} \quad (3.35)$$

$$[\bar{F}_{R_y\Pi}]_{k,l} = \begin{cases} b_2 \sum_{i \in H(k)} \frac{(y_k - y_i)}{2d_{k,l}^2} & k = l \\ -b_2 I_{H(k)}(l) \frac{(y_k - y_i)}{2d_{k,l}^2} & k \neq l \end{cases} \quad (3.36)$$

$$[\bar{F}_{R_z\Pi}]_{k,l} = \begin{cases} b_2 \sum_{i \in H(k)} \frac{(z_k - z_i)}{2d_{k,l}^2} & k = l \\ -b_2 I_{H(k)}(l) \frac{(z_k - z_i)}{2d_{k,l}^2} & k \neq l \end{cases} \quad (3.37)$$

$$[\bar{F}_{R_{yx}}] = [\bar{F}_{R_{xy}}]'; \quad [\bar{F}_{R_{zx}}] = [\bar{F}_{R_{xz}}]'; \quad [\bar{F}_{R_{zx}}] = [\bar{F}_{R_{xz}}]; \quad [\bar{F}_{R_{\Pi x}}] = [\bar{F}_{R_x\Pi}]'; \quad [\bar{F}_{R_{\Pi y}}] = [\bar{F}_{R_y\Pi}]';$$

$$[\bar{F}_{R_{\Pi z}}] = [\bar{F}_{R_z\Pi}]'$$

$$\text{Where } b_1 = 2(10\alpha)^2 / ((1+\rho) \sigma_{dB}^2 (\log 10)^2),$$

$$b_2 = (20\alpha) / ((1+\rho) \sigma_{dB}^2 \log 10),$$

$$I_{H(k)}(l) = 1 \text{ if } l \in H(k) \text{ and } 0 \text{ otherwise}$$

$$d_{ij} = \sqrt{(x_i - x_j)^2 + (y_i - y_j)^2 + (z_i - z_j)^2}$$

In the similar manner the elements of F_{θ}^{Δ} are given by:

$$[F_{R_{mn}}^{\Delta}]_{k,l} = \begin{cases} \sum_{i \in H(k)} \frac{1}{b_3}, & k = l \\ -\frac{I_{H(k)}(l)1}{4b_3} & k \neq l, \text{ when } m = n = \Pi \\ 0, & \text{otherwise} \end{cases} \quad (3.38)$$

$$\text{Where } b_3 = 2(1 + \rho) / \alpha^2$$

3.6 Analysis of the Bounds

In this section, we examine the lower bounds for different organs with a certain degree of variance in the transmitted power. We simulated the above equations in MATLAB. In these simulations, for simplicity, it is assumed that the radio range for any two sensors communicating is infinite, i.e., every sensor is able to communicate with every other sensor considered in the scenario. For analysis of the simulations we calculate the RMSE localization error using the formula

$$\bar{\sigma}_r^2 = \frac{1}{n} \text{tr}(\mathbf{F}_r^{-1}) \quad (3.39)$$

3.6.1 Problem Formulation and Simulation Scenario

The scenario considered for simulations consists of sensors placed on the jacket worn by the patient under observation as shown in Figure 7. The configuration of the sensors on the jacket, which form an array of anchor nodes for cooperative localization, is discussed in the next subsection. The sensor in the capsule traversing the GI track, which is supposed to be localized, is assumed to be a blind node. By blind node we refer to a sensor node whose coordinates are to be estimated using anchor nodes, which are placed on the jacket worn by the patient. We denote the number of anchor nodes by m and number of blind nodes (i.e., capsules) by n . Thus, the problem consists of calculating the Bayesian CRB of the capsule sensor coordinates, $\mathbf{r}_i = [x_i; y_i; z_i]$ for $i = 1$ to n as the capsule passes through the human digestive track, consisting of stomach, small intestine, and large intestine, with the help of a priori known co-ordinates $\mathbf{r}_i = [x_i; y_i; z_i]$ for $i = n+1$ to N , where $N = n + m$. We use a 3D human body model from full-wave electromagnetic

field simulation software, namely HFSS [65], to get coordinates of the capsule at different positions inside three main digestive organs in human GI track. We assume each receiver sensor can measure the RSS from all other sensors. Let $H(i) = j$: device j makes pairwise measurements with device i . These sensors are placed with same configuration in the front and the back of the jacket forming the anchor nodes and the sensor on the capsule is the blind node of the cooperative localization problem. We do the analysis of finding the CRB with 16, 32, 64, and 128 sensors on the jacket. We calculate the localization bounds using the RF triangulation method.

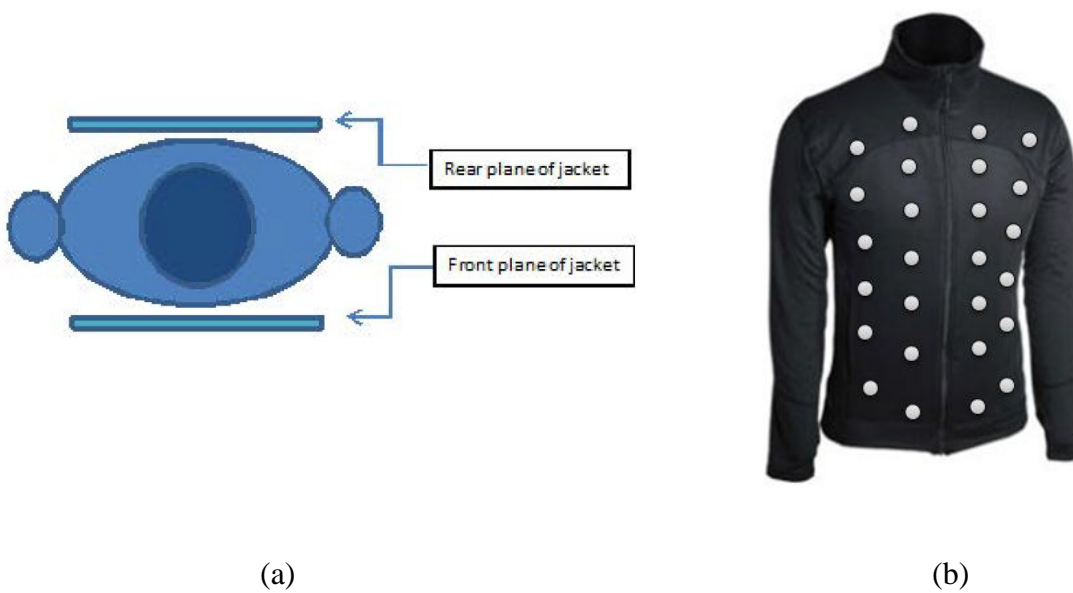


Figure 7: Simplified Diagram of the simulation setup: a) Top View of the human body with jacket sensor planes, b) A front view of a jacket with sensors placed on it

3.6.1.1 Sensor configuration:

In the simulation, four different sensor populations on the jacket are considered, namely 16, 32, 64, and 128. For each of these sensor population three different sensor placements are considered which represents potential sensor arrangement in practice as shown in Figure 8. Half the

numbers of the sensors are on the front plane of the jacket and half of them are in the back (rear) plane of the jacket. As you could see, these sensor configurations can be seen to have three distinct forms namely, Config1: sensors uniformly distributed in both the planes of the jacket, Config2: sensors concentrated at the center of the jacket, and Config3: sensors concentrated at the borders of the jacket. Figure 9 shows the Root Mean Square Error (RMSE) of the three different sensor populations for all three configurations. It can be observed that better performance is achieved when the sensors are concentrated near the center of the jacket. Arranging all the sensors concentrating on the boundary should be avoided since such a configuration performs the worst.

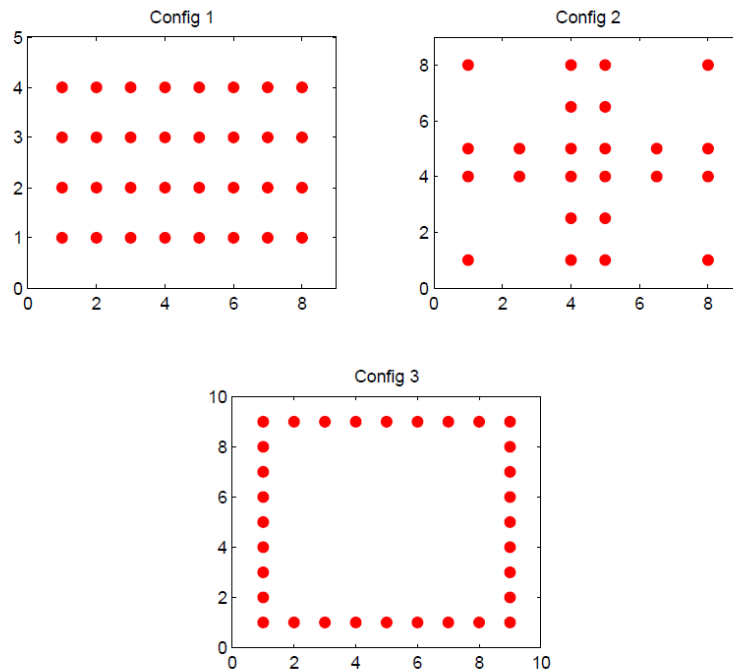


Figure 8: Three Sensor configurations on the jacket of patient considered for analysis of the bounds (Number of sensors = 64 with 32 sensors in the front and back plane); Config1: Sensors uniformly distributed; Config2: Sensors concentrated at center; Config3: Sensors Concentrated at edges

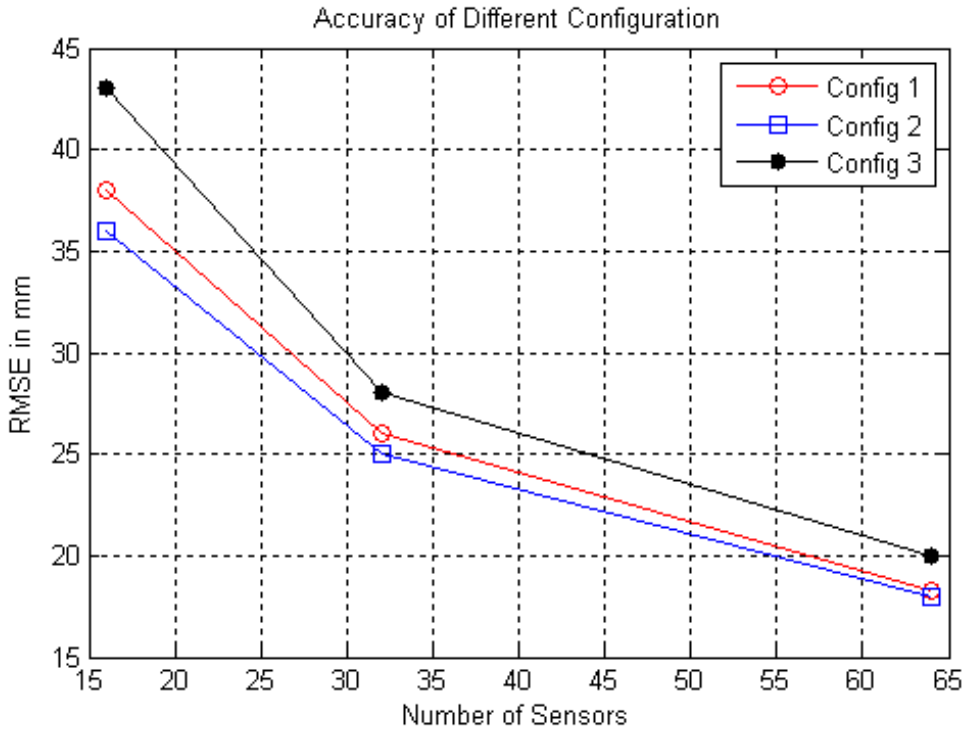


Figure 9: Localization Performance for the configurations shown in Figure 8 as a function of number of sensors

3.6.2 Performance Bounds in different Organs

In this Section, we calculate the bounds for different organs that form GI track. We plot the lower bound on the $1-\sigma$ uncertainty ellipse for \hat{r}_i , the estimate of the i^{th} capsule sensor coordinate. In this example, we use $\sigma_{\text{dB}} = 7.85$ and $\alpha = 4.26$ based on the path loss model discussed in the previous Section 3.4. For the current simulation, we consider $\rho = 0.704$ and sensor configuration number 2. The bounds are seen to have similar behavior at different values of ρ . In later sections of the simulation results, we will examine the bounds as a function of ρ . Finally, in these examples, the prior knowledge of transmit power is $\sigma_{\Pi} = 10$ dBm based on the explanations provided in [62]. We also consider the case when $\sigma_{\Pi} = 0$ dB for the purpose of comparison. For perfectly known transmit power (i.e., $\sigma_{\Pi} = 0$ dB), the uncertainty ellipse is

shown by solid lines whereas, for $\sigma_{\Pi} = 10\text{dBm}$ it is shown by dotted lines. As we can see in the Table IV, the increase in the RMSE for all three organs when randomness in the transmit power exists. Figure 10 shows corresponding bound in each organ individually. It is observed with the given configuration of anchor nodes, capsules in large intestine suffered the largest localization error when there was variance in transmit power. For the small intestine, the value of RMSE for $\sigma_{\Pi} = 0\text{dB}$ was 22.1399mm and for $\sigma_{\Pi} = 10\text{dBm}$ was 22.4024mm i.e. an increase in error of about 1.1.

Table IV: Percentage Increase in the RMSE (mm) of the Capsule in Three Different Organs of the GI Track [63]

Human Organ	$\sigma_{\Pi} = 0\text{dB}$	$\sigma_{\Pi} = 10\text{dBm}$	% increase
Stomach	20.8284	21.8090	4.7
Small Intestine	22.1399	22.4024	1.2
Large Intestine	26.2381	28.0591	7.1

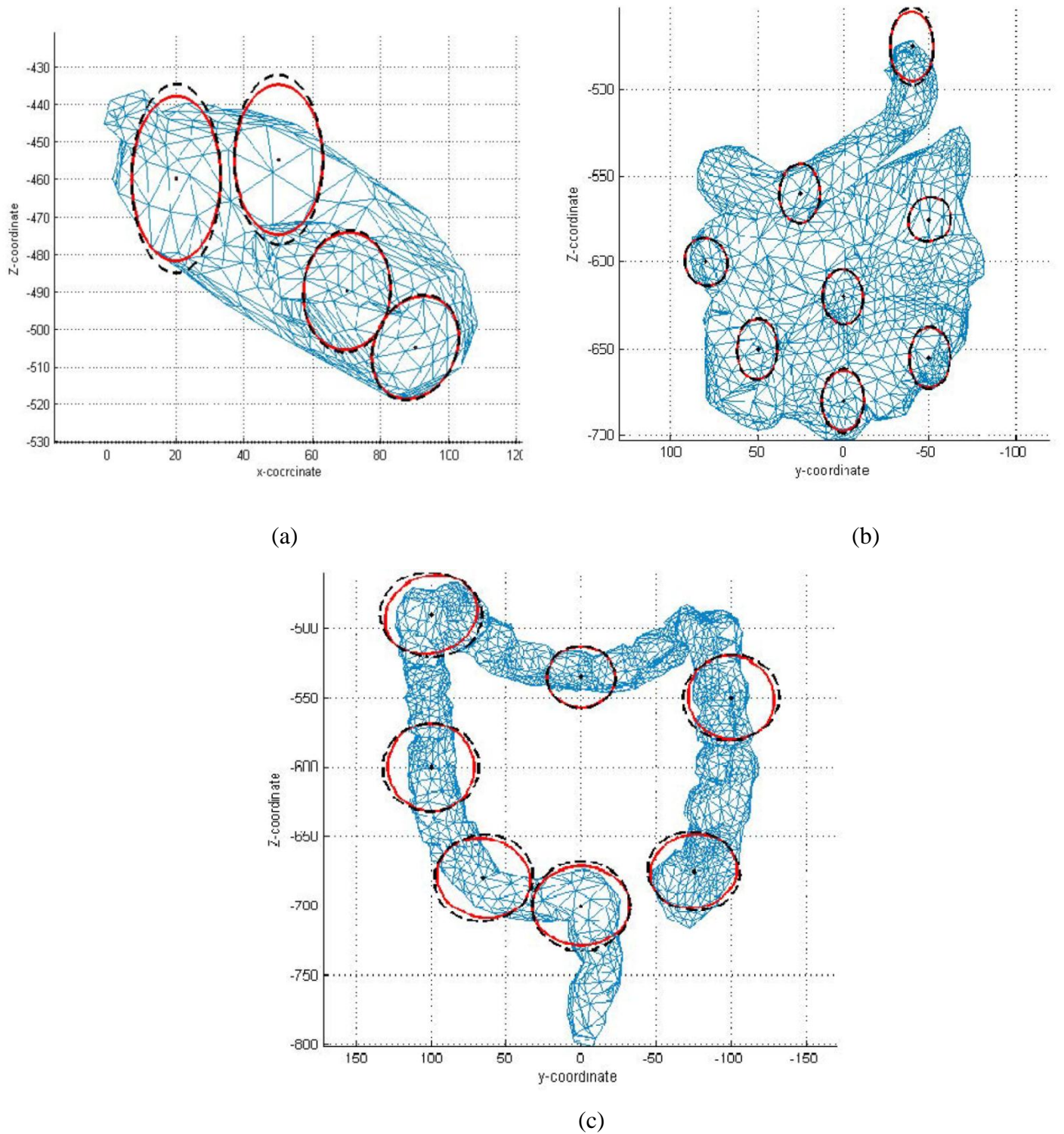


Figure 10: Comparison of Bayesian CRB on $1\text{-}\sigma$ uncertainty ellipses (left: Stomach Middle: Small Intestine Right: Large Intestine) when transmitted power is perfectly known (Solid line in red) or random with $\sigma_{\Pi} = 10\text{dBm}$. (Dashed lines in Black), for different unknown capsule locations (.)

3.6.3 Performance as a Function of Number of Sensors

In this Section, we investigate the impact of number of on-body sensors on the localization accuracy with and without power variance. In this experiment, 1000 Monte Carlo simulations in all the three organs (Stomach, Small Intestine, and Large Intestine) were carried out with number of sensors 16, 32, 64, and 128. During the simulation, we assume that the single capsule to be localized is located randomly in one of the three organs.

The results show that number of sensors has a significant impact on the accuracy with which the capsule can be localized. We use sensor placement configuration number 2 as discussed in Section 3.6.1.1 for simulation. Figure 11 shows the RMSE for all three organs as a function of number of sensors. It was observed that Large Intestine has the largest RMSE for a given configuration of sensors whereas; small intestine has the best accuracy. Thus, the large Intestine is a harsher implant environment for RF localization, requiring a larger number of receiver sensors on the body surface to achieve the same localization performance. As we can see, the variance in power causes higher RMSE at lower number of sensors. In general, we observe that as number of sensors increases (above 64 sensors), the randomness in the transmitted power has a lesser impact on the performance of the localization bounds.

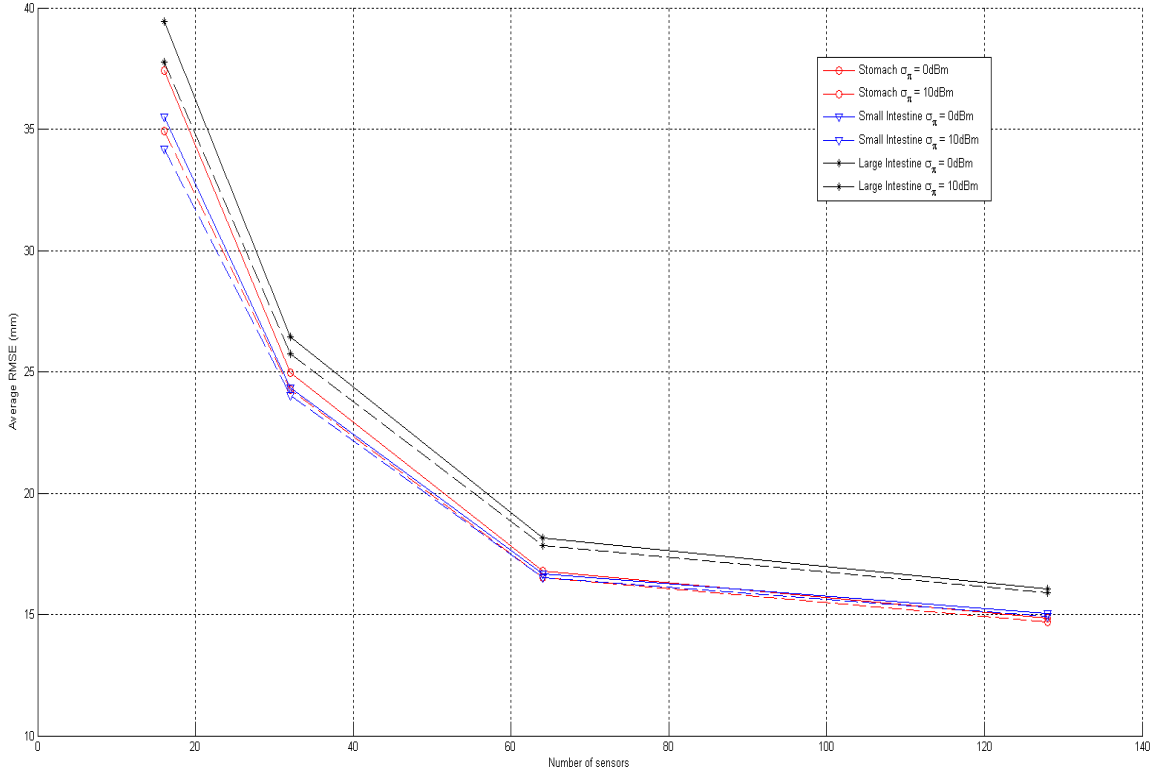


Figure 11: Localization performance (RMSE) as a function of number of receiver sensors in different organs ($\sigma_{\text{dB}} = 7.85$ and $\alpha = 4.26$)

3.6.4 Performance as a Function of ρ and σ_{Π}

Finally, we calculate the bound over the entire range of correlation coefficient values. Here, we have used a grid of 64 sensors with configuration number 2. The rest of the parameters are kept the same as in the previous simulations. In this experiment, the capsule is assumed to be in any one of the three organs and the average performance bounds as a function of ρ is calculated. As seen in Figure 12, as $\rho \rightarrow 1$ the lower bounds are not affected with randomness in transmitted

power as much as at lower values of ρ . Also at lower values of ρ , the RMSE is lower than that at the higher values.

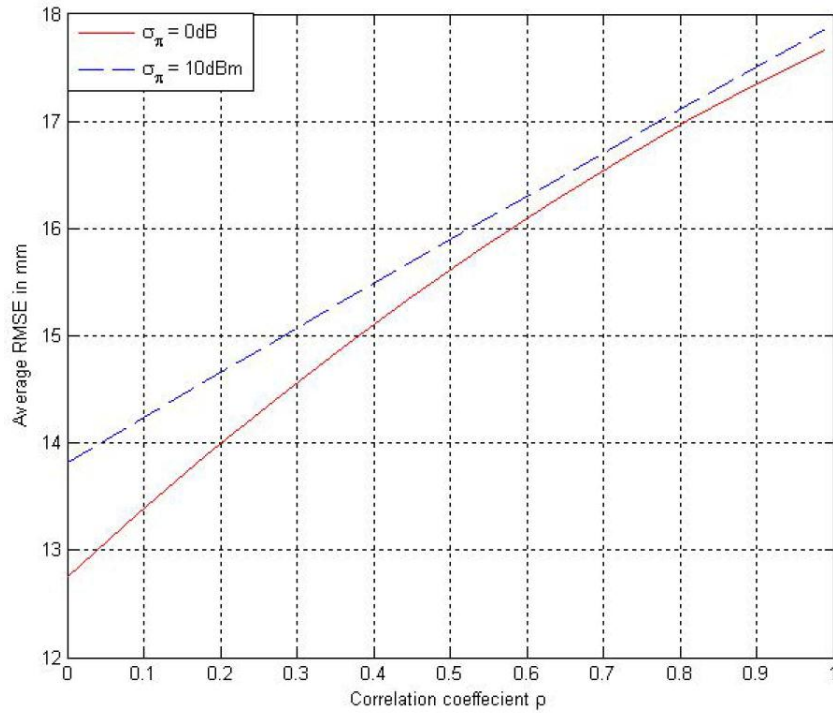


Figure 12: Bayesian CRB bounds for σ_r for 64 sensor configuration for two values of σ_{Π} and a range of ρ ($\sigma_{\text{dB}} = 7.85$ and $\alpha = 4.26$)

Chapter 4

Fast FDTD Simulation Techniques for analysis of TOA based Localization

4.1 Introduction

The finite-difference time-domain (FDTD) method [66] has been proven to be an effective simulation method that provides accurate predictions of field behaviors for varieties of electromagnetic interaction problems. In the FDTD method, Maxwell's curl equations are discretized by utilizing central-difference equations with second-order accuracy, with the electric and magnetic field components located at the suitable position on the Yee cell [67]. Traditionally, FDTD simulations have been widely used as a computation technique for determining the wave propagation for indoor localization, geolocation and channel modeling.

Measurements along with FDTD simulations have been the center of focus for several research papers in the past for determining the accuracy of indoor geo-localization using RSS or TOA, but when it comes to body area networks, the measurements becomes more and more challenging due to the several specifics of the human body medium and its applications that are profoundly different from the traditional indoor radio propagation challenges. Also it is practically impossible to go inside the human body or have a sensor placed inside the human body to determine the characteristics of the wireless waveform transmissions within the human body. Moreover, measurements are expensive, time consuming and hardly repeatable; hence FDTD computational technique becomes the natural choice for simulations to determine the wave propagation and to analyze the radiation characteristics of implanted devices inside the human body.

A Body Area Network (BAN) as we have described before is a conceptual term for a network technology targeted for use in or around the human body. Two competing applications driving this development are medical applications (e.g. implants) and entertainment. The BAN system used for medical applications is generally referred to as implanted Body area networks, which consists of a number of Nano-size wireless communication devices using sophisticated semiconductor technology capable of communicating with each other forming a sensor network inside the human body for health monitoring purpose. In [68], a global overview of implanted microsystems, and their clinical application is presented, and it is shown that at the current stage, implanted devices can be almost everywhere inside the human body. To ensure wireless connectivity of such implanted systems with external base stations, accurate understanding of the radio propagation channel, including the effect of the antenna is necessary [68] [69]. The electrically small size of the commonly deployed implanted antennas, together with the body

losses, makes the electromagnetic analysis of the wireless communication extremely complicated and difficult. The aim of this study is to characterize the accuracy with which localization of the implanted devices can be achieved using the TOA information.

A major emphasis within the computational electromagnetics (CEM) community concerns the solution of Maxwell's differential equations using finite-difference time-domain (FDTD) techniques. Because of the computational time and memory requirements associated with these time-stepping algorithms, their application to very large problems has been somewhat limited. To alleviate these computational obstacles, some efforts have been aimed at the implementation of space-parallelism and concurrent computation of unknowns at different points in the spatial mesh using multiple processors [70]. For these schemes, however, communication and synchronization requirements have limited the amount of computational speed-up provided by the use of additional processors. In this part of thesis we discuss how this computational efficiency can be improved using a much simpler approach to this problem.

4.2 FDTD for waveform Transmission

Among all the numerical techniques aiming at solving Maxwell's equations, the Finite Difference Time Domain (FDTD) method [71] is arguably the most popular method in the past twenty years for the solution of electromagnetic problems. As first proposed by K. S. Yee in 1966, the FDTD method is a simple and elegant way to discretize the differential form of Maxwell's equations. Yee used an electric Field (\vec{E}) grid, which was offset both spatially and temporally from a magnetic Field (\vec{H}) grid to obtain the update equations that yield the near Fields at the present time step throughout the computational domain in terms of the Fields of the past time step. The

update equations are used in a leapfrog scheme to incrementally march the \vec{E} and \vec{H} fields forward in time.

After more than 30 years of development, the FDTD method has gone through thorough studies and been improved and refined in many ways from the choice of grid size and shape to the absorbing boundary conditions (ABCs). It has become well established and used widely in the modeling of all kinds of electromagnetic problems such as propagation, scattering and radiation.

FDTD as a numerical method has the advantage of being physically straight forward, mathematically simple and easy to implement. The leapfrog time-stepping procedure is fully explicit, therefore completely avoiding the problems involved with simultaneous equations and matrix inversion (which the Method of Moment needs). The FDTD method has the advantage of being capable of investigating geometrically complex objects in great detail. It is accurate and versatile. The FDTD method can model virtually any type of material of importance to electromagnetic technology. The near-to-far-Field transformation allows calculation of the complete far-field radiation pattern in a single FDTD run. The use of an impulse excitation in the time domain permits antenna characteristics to be calculated across a broad frequency spectrum from a single FDTD run via a concurrently computed Fourier transform [72]. The availability of both time domain and frequency domain data allows much physical insight into a problem by drawing on knowledge from two different perspectives. Further, the visualization of the Fields in time provided by FDTD lends physical insight into antenna radiation. However, due to the substantially large amount of computer resources required to implement it, the FDTD method always suffers from serious limitations when dealing with electrically large objects.

4.2.1 Basic Theory:

Maxwell's equations are the basic equations governing any electromagnetic problem. Considering an isotropic lossless and source free region of space, using the MKS units, the time dependent Maxwell's equations are given in differential form by [73]

$$\begin{aligned}\nabla \cdot \vec{D} &= \rho \\ \nabla \cdot \vec{B} &= 0 \\ \nabla \times \vec{E} &= -\mu \frac{\partial \vec{H}}{\partial t} \\ \nabla \times \vec{H} &= \varepsilon \frac{\partial \vec{E}}{\partial t} + \vec{J}_s\end{aligned}\tag{4.1}$$

Where, $\vec{D} = \varepsilon \vec{E}$: Electric flux density vector (C/m²)

$\vec{B} = \mu \vec{H}$: Magnetic Flux Density Vector (W/m²)

\vec{E} = Electric Field vector (V/m)

\vec{H} = magnetic Field vector (A/m)

μ = magnetic permeability (H/m)

ε = Electric permittivity (F/m)

\vec{J}_s = Electric current density (A/m²)

By writing out the vector components of the curl operators a system of six coupled scalar equations equivalent to Maxwell's curl equations in the three-dimensional rectangular coordinate system (x, y, z) can be obtained.

$$\frac{\partial E_x}{\partial t} = \frac{1}{\varepsilon} \cdot \left(\frac{\partial H_z}{\partial y} - \frac{\partial H_y}{\partial z} \right)$$

$$\begin{aligned}
\frac{\partial E_y}{\partial t} &= \frac{1}{\varepsilon} \cdot \left(\frac{\partial H_x}{\partial z} - \frac{\partial H_z}{\partial x} \right) \\
\frac{\partial E_z}{\partial t} &= \frac{1}{\varepsilon} \cdot \left(\frac{\partial H_y}{\partial x} - \frac{\partial H_x}{\partial y} \right) \\
\frac{\partial H_x}{\partial t} &= \frac{1}{\mu} \cdot \left(\frac{\partial E_y}{\partial z} - \frac{\partial E_z}{\partial y} \right) \\
\frac{\partial H_y}{\partial t} &= \frac{1}{\mu} \cdot \left(\frac{\partial E_z}{\partial x} - \frac{\partial E_x}{\partial z} \right) \\
\frac{\partial H_z}{\partial t} &= \frac{1}{\mu} \cdot \left(\frac{\partial E_x}{\partial y} - \frac{\partial E_y}{\partial x} \right)
\end{aligned} \tag{4.2}$$

The system of six coupled partial differential equations given above forms the basis of the FDTD numerical algorithm for electromagnetic wave interactions with general three-dimensional objects. The FDTD algorithm needs not explicitly enforce the Gauss's law relations indicating zero free electric and magnetic charge because these relations are theoretically a direct consequence of the curl equations.

4.2.2 Yee Algorithm

Yee employed finite difference notations introduced in the previous section to solve for Maxwell's curl equations numerically in the time domain [67]. The method is based on the approximation of partial derivatives in a regular grid of points by means of central finite differences, which resulted in the Yee algorithm [67]. The partial derivatives of Maxwell's curl equations can be derived following the second order finite difference scheme described above, resulting in a set of discrete difference equations. The FDTD equations for the E_x and H_y components are shown respectively in following equations

$$E_x^{n+1}|_{i,j,k} = E_x^n|_{i,j,k} + \frac{\Delta t}{\varepsilon} \left[\frac{(H_z^{n+1/2}|_{i,j+1/2,k} - H_z^{n+1/2}|_{i,j-1/2,k})}{\Delta y} - \frac{(H_y^{n+1/2}|_{i,j,k+1/2} - H_y^{n+1/2}|_{i,j,k-1/2})}{\Delta z} \right] \quad (4.3)$$

$$H_z^{n+1}|_{i,j,k} = H_z^n|_{i,j,k} - \frac{\Delta t}{\varepsilon} \left[\frac{(E_y^{n+1/2}|_{i+1/2,j,k} - E_y^{n+1/2}|_{i-1/2,j,k})}{\Delta x} - \frac{(E_x^{n+1/2}|_{i,j+1/2,k} - E_x^{n+1/2}|_{i,j-1/2,k})}{\Delta y} \right] \quad (4.4)$$

It can be seen from the above equations that the FDTD method solves for both the electric and magnetic fields using Maxwell's curl equations rather than solving for the electric field (or the magnetic field alone) with a wave equation. Each field component in the set of finite difference equations is related to the field components in a previous time instant. As a result, the equation system can be solved by iteration, provided that the initial conditions for the fields are known.

At each iteration of time step, the field is updated in a time instant later than the original one. The iterative method is known as the Yee algorithm. In principle, this algorithm is simply based on Maxwell's curl equations, but the divergence equations are automatically fulfilled by the discrete system [67].

4.2.3 Yee Grid

As a consequence of the central finite difference scheme, the electric field components have to be located in the middle of the magnetic field components in order to compute the central finite differences (or vice versa). This means that the continuous field has to be sampled alternatively in space with the proper field component. It can be seen from Figure 13, that the Yee algorithm centers its electric field \vec{E} and magnetic field \vec{H} components in a 3-D space so that every \vec{E} component is surrounded by four circulating \vec{H} field points and vice versa as shown in Figure 13.

The magnetic and electric fields also have to be alternated in time for the same reason. This is the so-called 'leapfrog' arrangement. All the electric field \vec{E} in the 3-D space of interest are computed and stored in memory for a particular time instant using magnetic field \vec{H} data previously stored in the computer memory [67]. Following that all the magnetic field \vec{H} in the modeled space are computed and stored in memory using the \vec{E} data just computed. The cycle begins again with the recalculation of the \vec{E} components based on the newly obtained \vec{H} . This process continues until time stepping is concluded and steady state conditions are achieved.

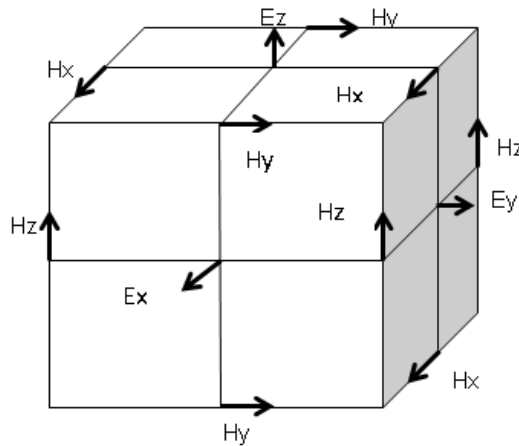


Figure 13: Yee Grid with every \vec{E} component surrounded by four circulating \vec{H} field points and vice versa

The Yee algorithm can be extended to handle most known media, such as lossy, dispersive and anisotropic material [67]. Anisotropic and inhomogeneous media can be modeled with just minor changes to the basic equations. As the FDTD method works in the time domain, non-linear and active device can be fully supported, although the iteration scheme to solve the finite difference equations are more complex than the basic ones described here.

4.2.4 Absorbing Boundary Condition

It can be seen from the previous sections that in order to update the fields at certain location, it is necessary to know the field values adjacent to it. In some problems, the structure of interest is 'close', so the fields at the boundary are determined and can be readily used to update the fields beside the boundary (e.g. waveguide, metallic enclosures). However, a lot of electromagnetic problems of interest are defined in 'open' regions where the spatial domain of the computed Field is unbounded in one or more coordinate directions. Since a real computer has a limited memory, it is not possible for it to store an unlimited amount of data. Therefore, the field computation domain must be limited in size. The computation domain must be large enough to enclose the structure of interest and a suitable boundary condition on the outer perimeter of the domain must be used to simulate its extension to infinity. In the process, the outer boundary condition must suppress spurious reflections of the outgoing numerical wave to an acceptable level. This would permit the FDTD solution to remain valid for all time steps, especially after the reflected wave return to the vicinity of the modeled structure. Depending upon their theoretical basis, this outer boundary condition is called either radiation boundary conditions (RBCs) or absorbing boundary conditions (ABCs). In this thesis the notation ABC is used.

ABCs cannot be directly obtained from the numerical algorithm for Maxwell's curl equations defined by the finite difference system. This is because the finite difference system employs a central spatial difference scheme that requires knowledge of the field one-half space cell to each side of an observation point. Central differences cannot be implemented at the outmost grid planes where there is no information concerning the fields at points one-half space cell outside of these planes. Scientists have tried various techniques to get ABCs with

satisfactory performance, which include approximation operators and artificial absorbing materials.

The proprietary FDTD software developed in our lab includes a first order Mur absorption boundary condition [78]. During the Waveform simulation and measurement comparison as will be discussed in the section 4.3, this basic first order ABC, resulted in reflection from the boundaries when simulated for wideband signals. Hence, a super absorption ABC was implemented. Super absorption is not an ABC by itself, but rather a numerical procedure for the improvement of the local ABC's applied to the FDTD technique. It embodies an error-canceling formulation according to which the same ABC is applied to both E and H field components on and near the outer boundaries, depending on the polarization examined.

Following is the part off the code which was modified to introduce super absorption to first order Mur's ABC [78].

```

Hy(1, :, :) = (rho*Hy(1, :, :) + Hy(1, :, :))/(1+rho); % x = 0;
Hy(Nx, :, :) = (rho*Hy(Nx, :, :) + Hy(Nx, :, :))/(1+rho); % x = Lx;
Hy(:, :, 1) = (rho*Hy(:, :, 1) + Hy(:, :, 1))/(1+rho);
Hy(:, :, Nz) = (rho*Hy(:, :, Nz) + Hy(:, :, Nz))/(1+rho);

Hx(:, 1, :) = (rho*Hx(:, 1, :) + Hx(:, 1, :))/(1+rho); % y = 0;
Hx(:, Ny, :) = (rho*Hx(:, Ny, :) + Hx(:, Ny, :))/(1+rho); % y = Ly;
Hx(:, :, 1) = (rho*Hx(:, :, 1) + Hx(:, :, 1))/(1+rho);
Hx(:, :, Nz) = (rho*Hx(:, :, Nz) + Hx(:, :, Nz))/(1+rho);

Hz(1, :, :) = (rho*Hz(1, :, :) + Hz(1, :, :))/(1+rho); % x = 0;
Hz(Nx, :, :) = (rho*Hz(Nx, :, :) + Hz(Nx, :, :))/(1+rho); % x = Lx;
Hz(:, 1, :) = (rho*Hz(:, 1, :) + Hz(:, 1, :))/(1+rho); % y = 0;
Hz(:, Ny, :) = (rho*Hz(:, Ny, :) + Hz(:, Ny, :))/(1+rho); % y = Ly;

```

4.3 Comparison of Waveform Simulation with Measurements

Here we make comparisons of simulation using our proprietary FDTD software programmed in MATLAB and empirical measurement in order to determine the accuracy of the simulation and how well fits the real empirical measurements and to ensure that the predictions based on the simulation are sufficiently reliable, that they correlate reasonably closely with the measurements, and, hence, are useful for developing propagation models that we can trust, without having to constantly go back to the Lab to undertake an extensive measurement program.

The measurement is done in an anechoic chamber using a vector network analyzer having a frequency range of operation up to 40 GHz. The anechoic chamber to a good extent represents the FDTD simulation environment which consists of a finite domain surrounded by absorption boundaries. The antennas used for the purpose of measurement was a quarter wave monopole antenna with ground plane as shown in lower right of Figure 20 which is similar to dipole antenna used in simulations as shown in lower left of Figure 20. The size of the dipole antenna used in simulations was flexible and it was fixed to match it to the monopole antenna.

First we match the measurements with the FDTD simulation results obtained in free space transmission, which match perfectly. We started by comparing the simulation and measurement in free space with bandwidth as low as 10MHz and grid size equal to 12.5 mm. Figure 14 gives the input signal of 84 MHz band to the simulation set up and Figure 15 gives the output at the receiving antenna 20 cm away. Figure 16 and 18, shows input signal at 700 MHz and 1GHz respectively, and Figure 17 and Figure 19 shows the output at the receiving antenna. Thus by observation, simulation gave acceptable results until the bandwidth goes to a certain point for a given grid size. We will discuss this issue in detail in Section 4.6.1 describing the bandwidth limitations of the FDTD simulation technique.

At ISM band of 84 MHz:

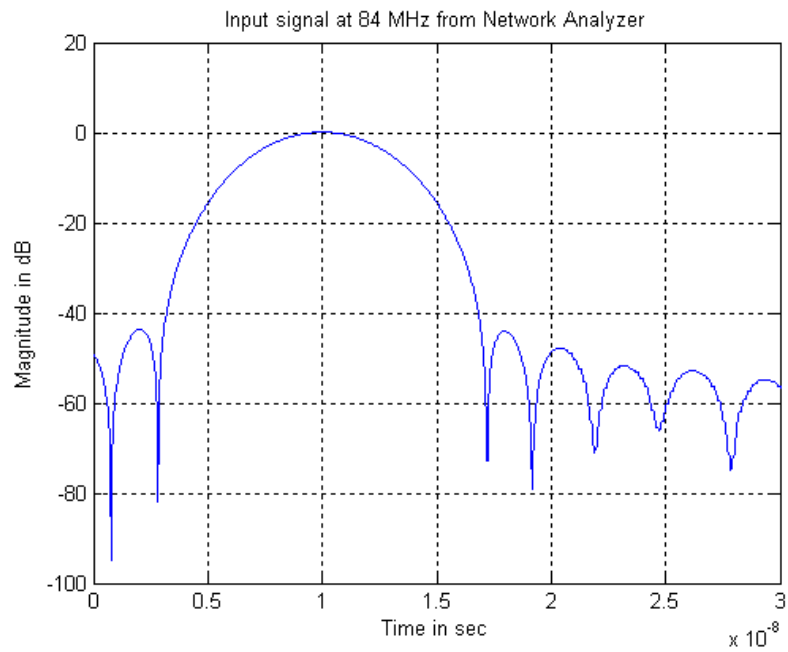


Figure 14: Input signal of 84MHz to the simulation setup

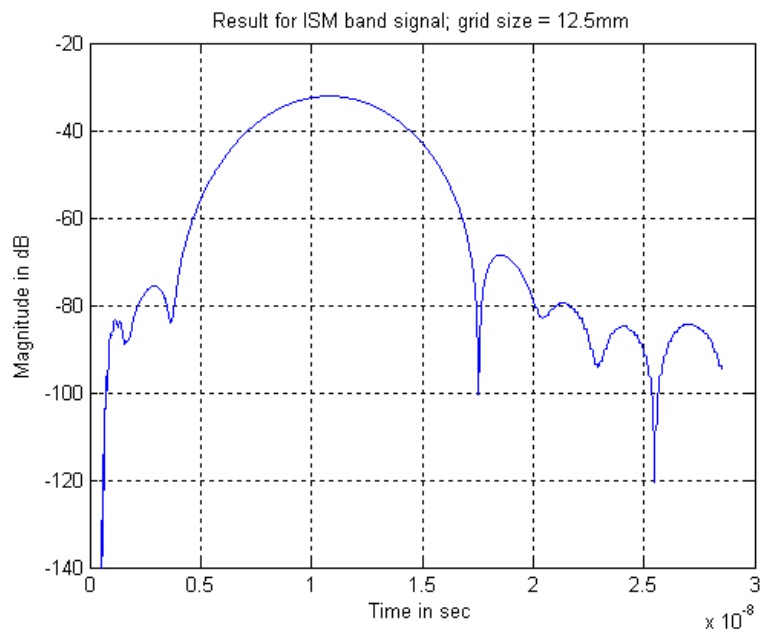


Figure 15: The result of simulation after inputting the 84MHz ISM band signal

At bandwidth of 700 MHz form 2.1MHz to 2.8MHz:

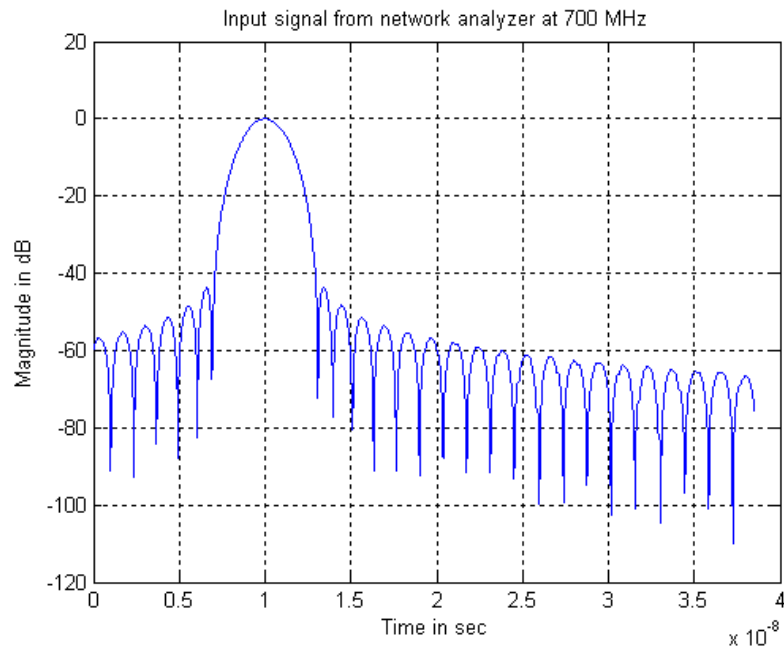


Figure 16: Input signal of 700 MHz to the simulation setup

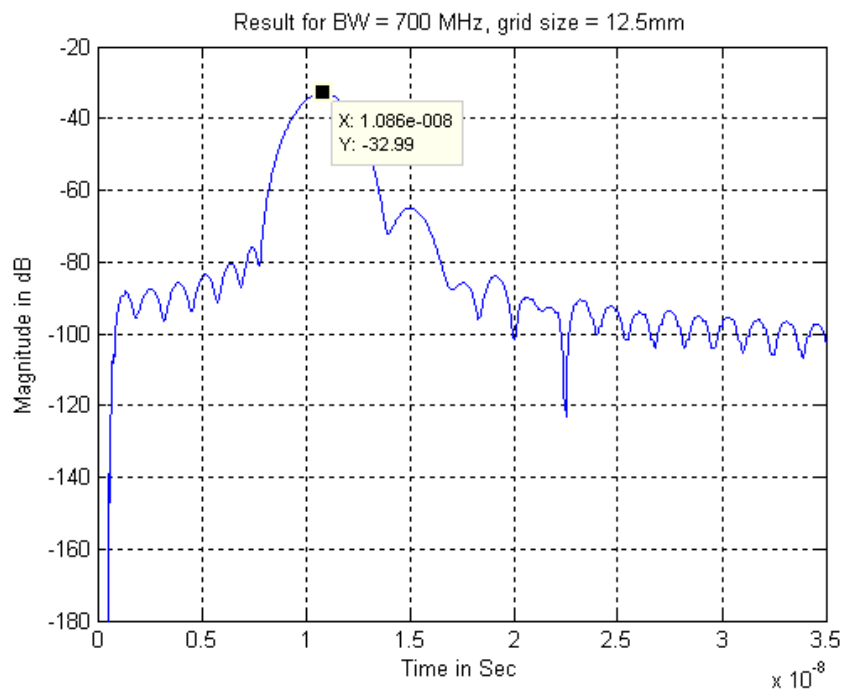


Figure 17: The result of simulation after inputting the 700 MHz band signal

At bandwidth of 1GHz form 2.1MHz to 3.1 MHz:

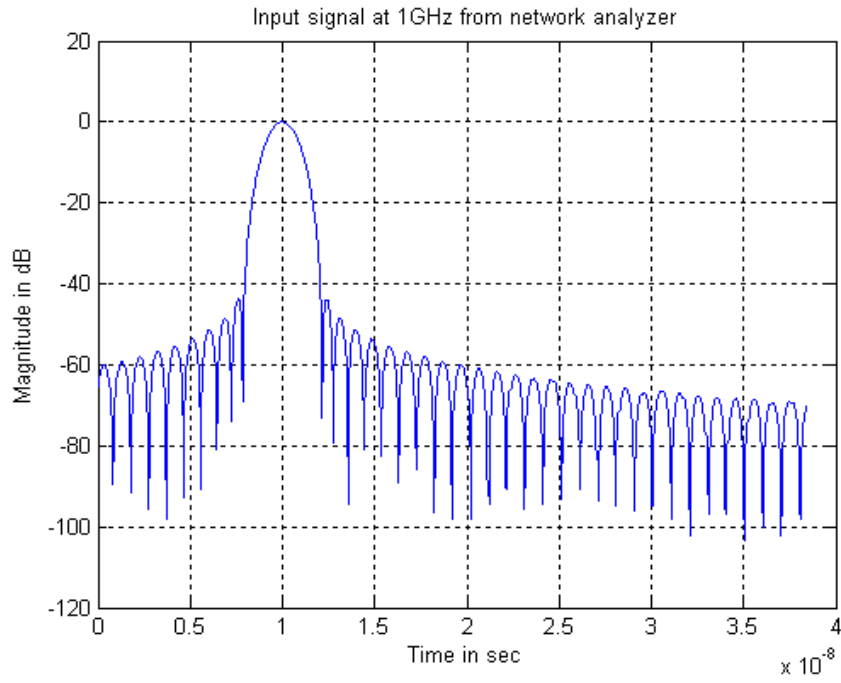


Figure 18: Input signal of 1GHz to the simulation setup

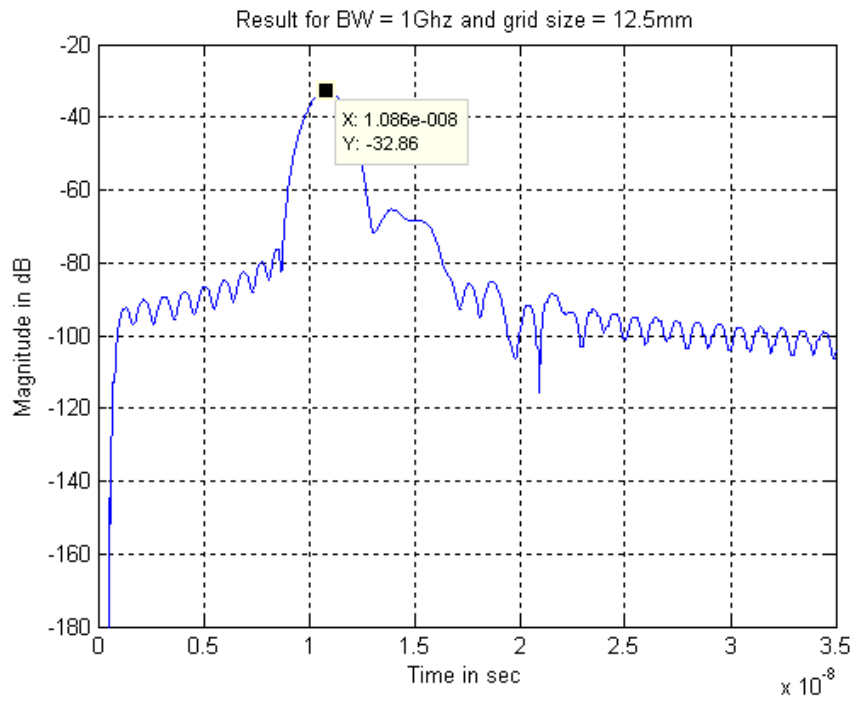


Figure 19: The result of simulation after inputting the 1GHz band signal

Thus it's quite clear that the FDTD software that we prepared performs best up to 100 MHz of bandwidth for a grid size of 12.5 mm and crashes if we try to simulate at a certain bandwidth beyond 100 MHz of bandwidth. Thus after validating the software we now move on to comparing the simulation set up and measurement using a hollow phantom which practically represents the exact characteristics of a normal human body. The phantom is shown in the Figure 20. The exact coordinates of the phantom for FDTD simulation were obtained from scanning the physical phantom at the U.S. Army Natick Laboratory near WPI.

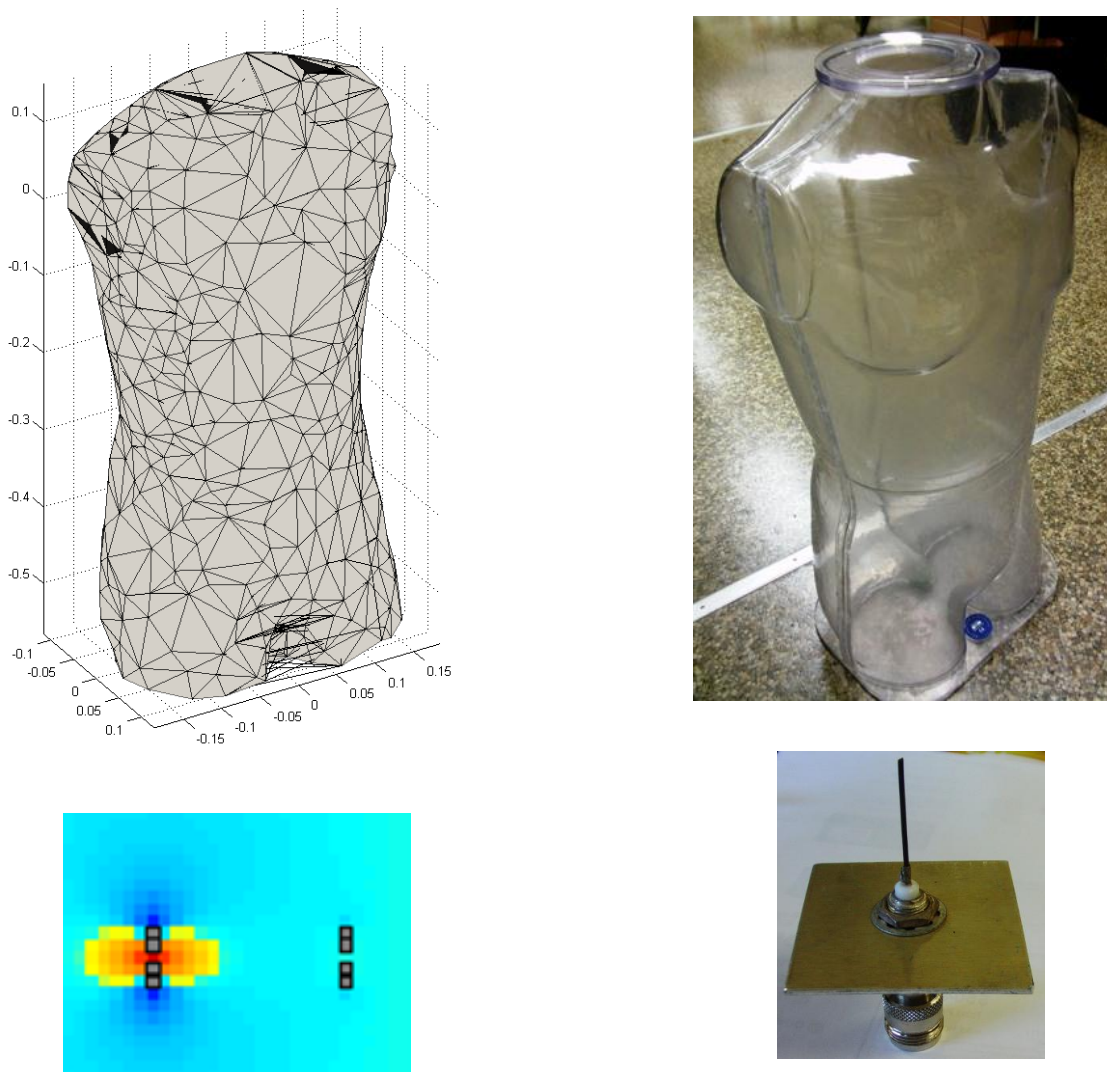
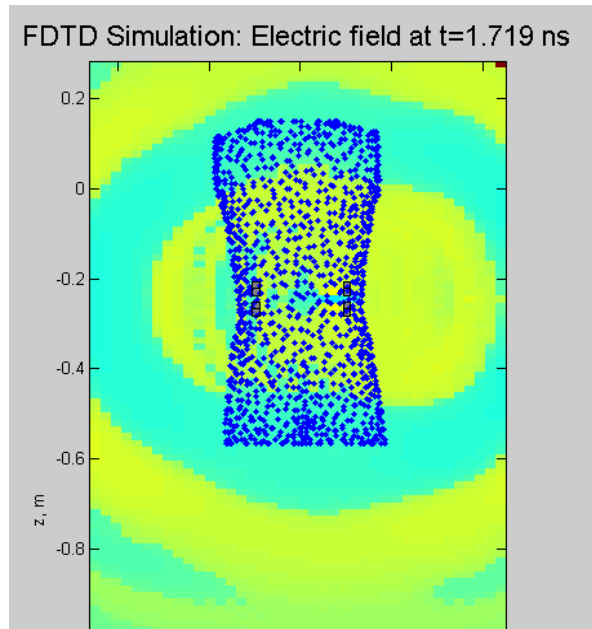


Figure 20: Picture of scanned Phantom Mesh (upper left) and physical Phantom (upper right) and antenna used for simulation (lower left) and measurement (lower right)

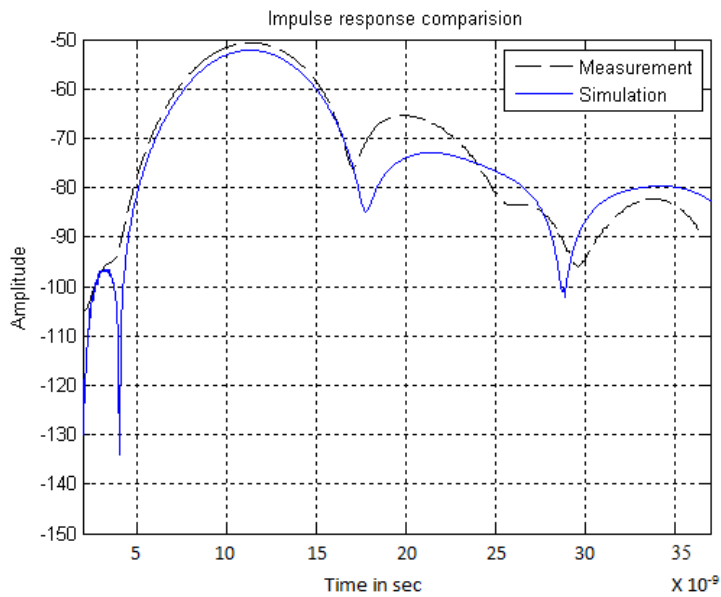
Now, the simulation and measurement is carried out in two more scenarios: a) with antennas placed on the front side surface of the phantom as in Figure 21; b) with the antenna placed on the front and back sides of the phantom as shown in Figure 22. In both the scenarios we use the ISM band 2.4GHz to 2.484GHz (which lies within the operational bandwidth of FDTD for a grid size of 12.5mm) as in this frequency band the simulation and measurement matched perfectly in free space.



(a)



(b)



(c)

Figure 21: Comparison of Simulation and Measurement with antennas placed in front of phantom; a) and b) gives the scenario and c) gives comparison result

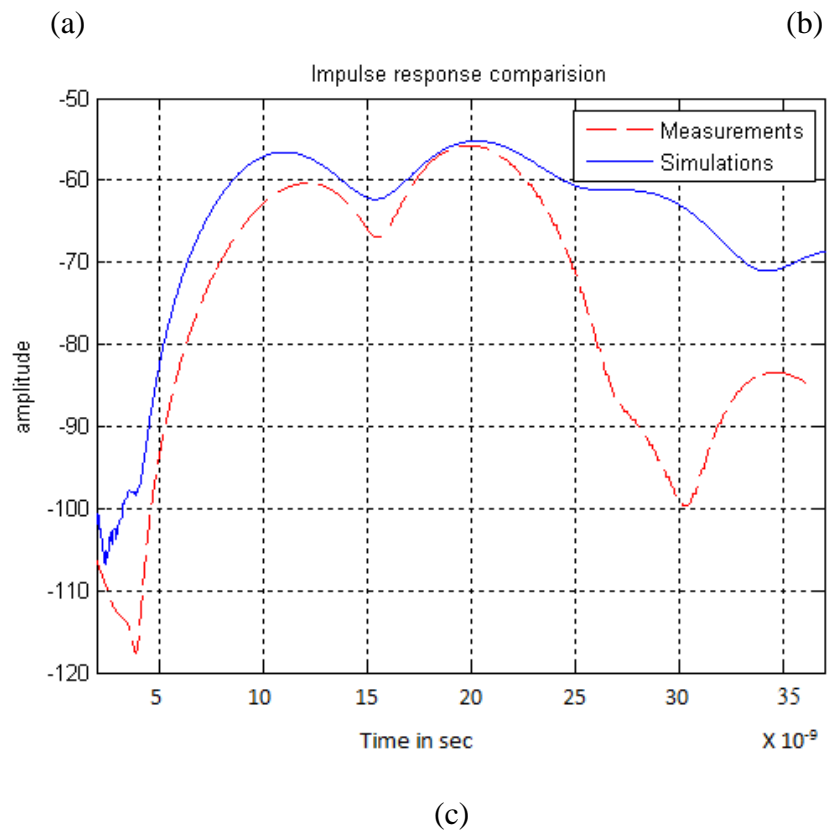
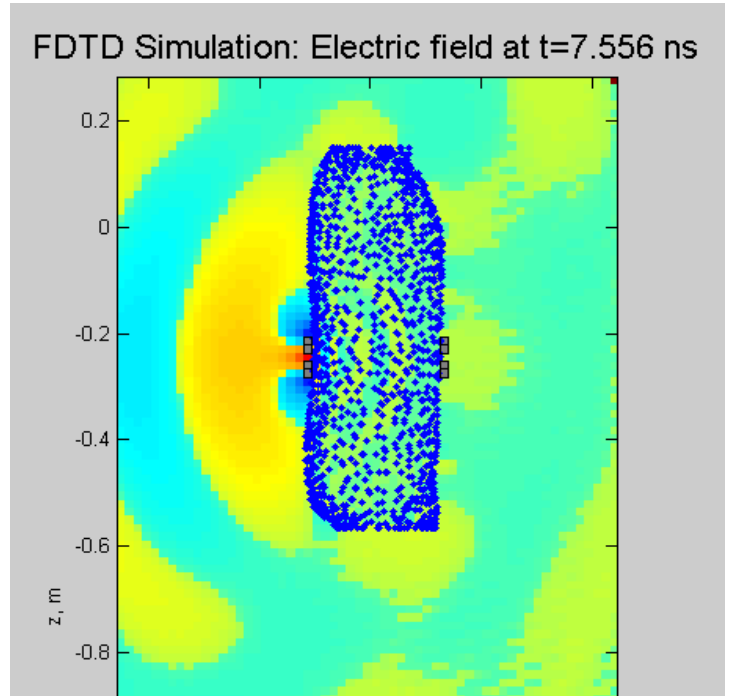


Figure 22: Comparison of Simulation and Measurement with antennas placed in front and back of phantom; a) and b) gives the scenario and c) gives the comparison result

As can be seen in Figure 21 and Figure 22, there is a good match between the simulation and measurement. Thus we conclude that all the simulation we have done using the FDTD simulation software are in good agreement with the real time measurement if the bandwidth of the signal is well within the operational bandwidth of the simulation.

4.4 Computational Complexity

Despite its simplicity and flexibility, the FDTD is a computationally intensive technique that requires large computation memory and time for electrically small structure. Such intensive memory and CPU time requirements are mainly due to the following two modeling constraints [66]:

- 1) The spatial increment step must be small enough in comparison with the smallest wavelength (usually 10-20 steps per smallest wavelength) in order to make numerical dispersion errors negligible.
- 2) The time step must be small enough so that it satisfies the following CFL stability condition:

$$u_{\max} \Delta t \leq \left[\frac{1}{\Delta x^2} + \frac{1}{\Delta y^2} + \frac{1}{\Delta z^2} \right]^{-\frac{1}{2}} \quad (4.5)$$

Here u_{\max} , is the maximum wave phase velocity within the model. If the time step is larger than the value specified above, the FDTD scheme will become numerically unstable, leading to an unbounded numerical error as the FDTD solution marches.

In order to examine the computational complexity and the time required to run the entire simulation, we performed an experiment using our 3D FDTD equation implemented in MATLAB. Here we examine the performance as a function of the grid size. We perform a simulation in free space with point source antennas located at 20cm away from each other with

the sine wave given as an input to the transmitter antenna at frequency of 100MHz. The grid sizes considered here are 25mm, 12.5mm, 6.25mm. For the purpose of simplicity we have considered the grid size along all three axes to be same i.e., $x = y = z = \delta$, where δ is the grid size.

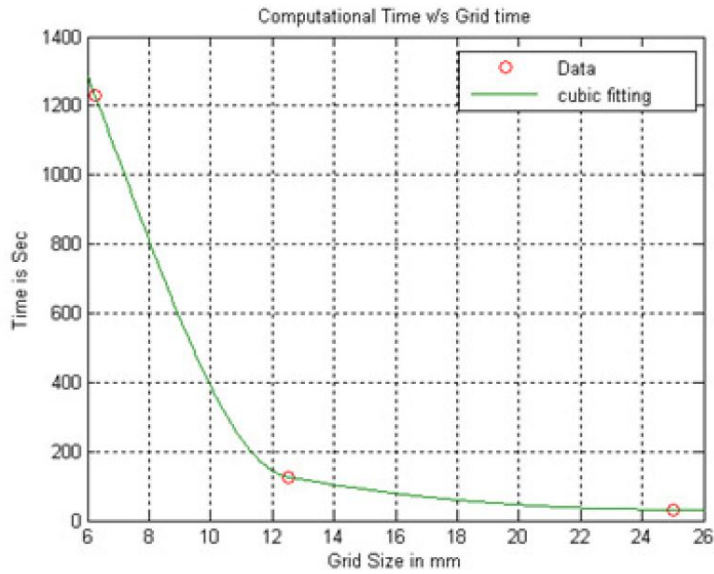


Figure 23: Computational time against grid size

Figure 23 shows the computational time required as a function of the grid size. It is very clear that as the grid size decreases, the increase in the computational time is not linear; instead the time required increase as a cubic power of the grid size.

Table V: Computational Complexity and Relative Ratio [74]

Domain Dimension	Grid Size (mm)	Time in sec	Relative ratio
192×192×192	6.25	1200	1
97×97×97	12.5	146	8
49×49×49	25	36	64

4.5 Fast Solution to FDTD using LTI analysis

From a signal processing point of view, the FDTD algorithm can be considered a Linear Time-Invariant (LTI) system which can be fully characterized by its transfer function. It is observed that, the output obtained at the receiving antenna after simulation is same as the convolution of the input signal with the impulse response of the system obtained with the same simulation settings. If we denote the impulse response by $h(n)$ then the simulation result of FDTD for any given input waveform $x(n)$ will be represented by the following

$$y(n) = \sum_{k=1}^N h(k)x(n - k) \quad (4.6)$$

The frequency response of the output is given by $Y(\omega) = H(\omega)X(\omega)$ where, $H(\omega)$ and $X(\omega)$ are given by:

$$H(\omega) = \sum h(n)e^{-j\omega n}; \quad X(\omega) = \sum x(n) e^{-j\omega n} \quad (4.7)$$

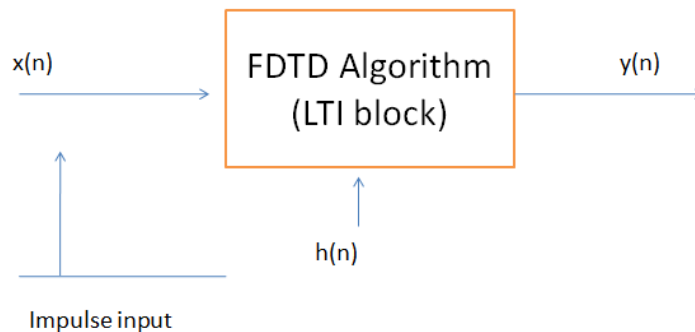


Figure 24: LTI system

The advantages of the LTI formulation are: a) If we simulate the impulse response between two points, we can obtain any other waveform transmission between those two points using convolution integral and save the computational time tremendously. b) We can use the Fourier Transform of the impulse response to determine the bandwidth limitations of the simulation. In particular, this method can be used determine the effect of bandwidth on the accuracy of TOA based localization, without running the FDTD simulation for hours.

Figure 25 provides a basic overview of how this mechanism works in case of FDTD. The input to the FDTD software is the waveform shown in the lower left part of the figure 25, having a bandwidth of 84 MHz (ISM band) and the output of the simulation is the waveform shown in the upper right side of the Figure 25. We then convolve the impulse response shown in the center bottom of the figure, obtained by keeping the same FDTD simulation setup with the input waveform and, we obtain the waveform shown in the lower right part of the figure. The outputs obtained from the two methods are identical concluding that the simulation can be interpreted as a LTI system. Using this approach for two locations in the body, for example, first we determine the impulse response with one simulation. After that the response to any other waveform with different bandwidths can be obtained without doing time consuming simulation and by simply convolving the input waveform with the impulse response of the system. Wireless Body area networks (WBAN) is an area whose standardization activity is underway, in such situations, highlighting the significance of bandwidth on the accuracy of localization inside human body becomes very important. Formulating FDTD as an LTI system simplifies this task by which the accuracy of time of arrival can be found by simply convolving the input wideband/narrowband signal with the impulse response.

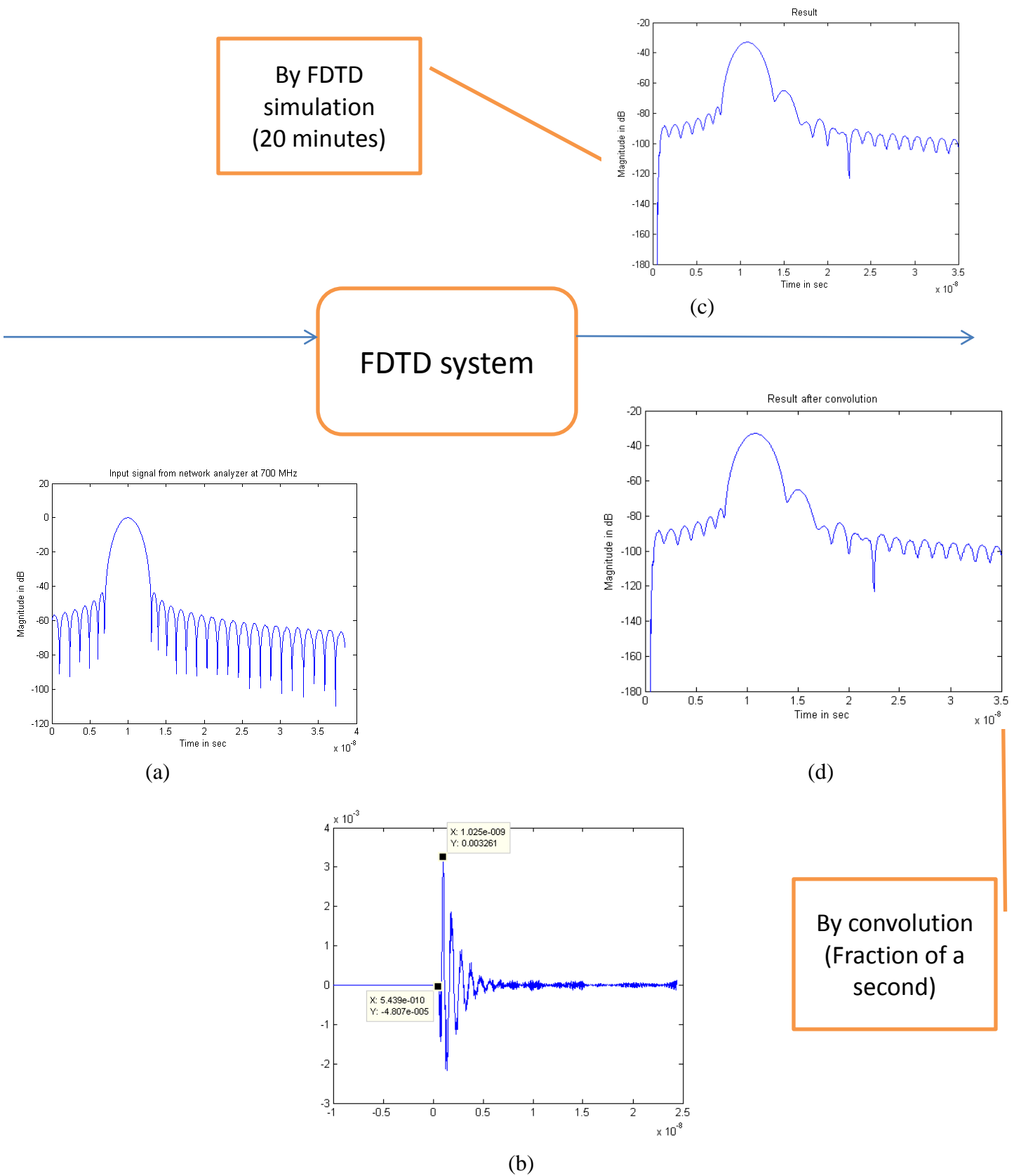


Figure 25: FDTD as Linear Time Invariant system; a) Input signal at 84 MHz; b) Impulse response of the FDTD system; c) The result obtained by actually running the simulation for around 20 min; d) the result within a fraction of a sec. by simply convolving signal in (a) and (b)

4.6 Efficient TOA Based Localization with BANs

Simulations are performed with transmitter and receiver placed at different points inside the body as shown in Figure 26. The 3D human body model used for the simulation has a spatial resolution of 2mm and is extracted from the three dimensional full wave electromagnetic field simulation system named HFSS (High Frequency Structure Simulator). For simplicity we have considered a uniformly homogeneous human body with a constant dielectric constant of $\epsilon_r = 50$.

The simulation points located inside the body takes into account the major part of the torso which is the most stable part as compare to other parts of the body, which are most of the time moving with respect to whole body. Since our simulation is static and does not consider the movement of the whole body, in general, understanding the behavior of the waveform transmission inside the torso is the most obvious option. The simulations were performed with the transmitter and receiver located at these points using a point source antenna. A point source antenna is an isotropic antenna which radiates equally in all directions. In Section 4.5, we discuss how a single impulse response can be used to characterize the transmission between any two of these points in the torso. Here we will apply this method to do some analysis and show some results.

4.6.1 Simulation Bandwidth as a Function of Distance

The FDTD method discussed has bandwidth limitations. For a given grid size, there is a maximum limit on the bandwidth for which the simulation gives acceptable results. If we consider the FDTD simulation as a LTI system represented by the channel impulse response, the Fourier

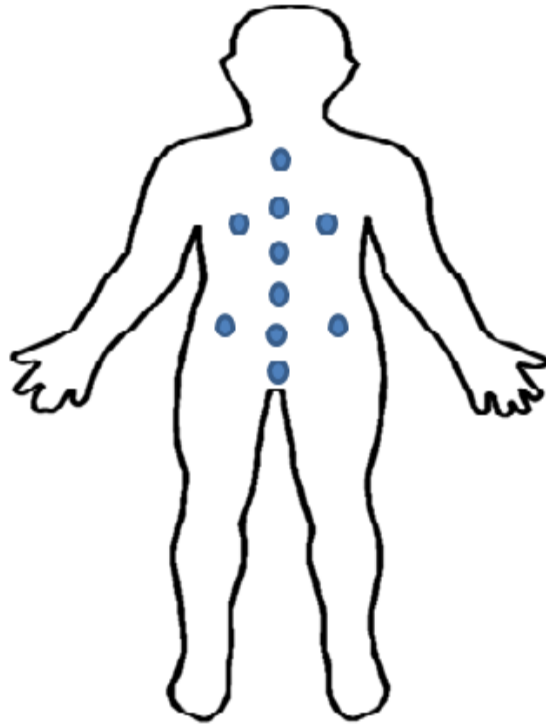


Figure 26: Simulation Scenario showing different points inside the torso where point source antennas were placed to carry out the simulation

transform of the impulse response represents the transfer function of the system, thereby illustrating the bandwidth of the simulation system. In this section we discuss how the distance between the two points inside human body affects the operational bandwidth. Since the impulse response changes as the distance between two simulated locations is increased, the bandwidth of the frequency response would be sensitive to the distance between two simulated points. To further elaborate on this point we considered the simulation scenario shown Figure 26. In this scenario, the transmitter antenna is fixed on the top point and the receiver is located at different points shown in the scenario. The top and bottom plots in Figure 27 shows the transfer function of the channel with receiver at second and third point from the top most point in Figure 26. Figure 28 shows how the bandwidth decreases as the distance between the two points increases. These results indicate that if we want to simulate using FDTD, we always have bandwidth

limitations that are a function of the distance. Figure 27 indicates that if the bandwidth of the transmitted signal for a grid size of 12.5mm is more than 850MHz, we cannot obtain accurate results using FDTD for a distance of 10cm between transmitter and the receiver. This is a very powerful conclusion, useful for practical aspects of simulations inside human body using the FDTD techniques.

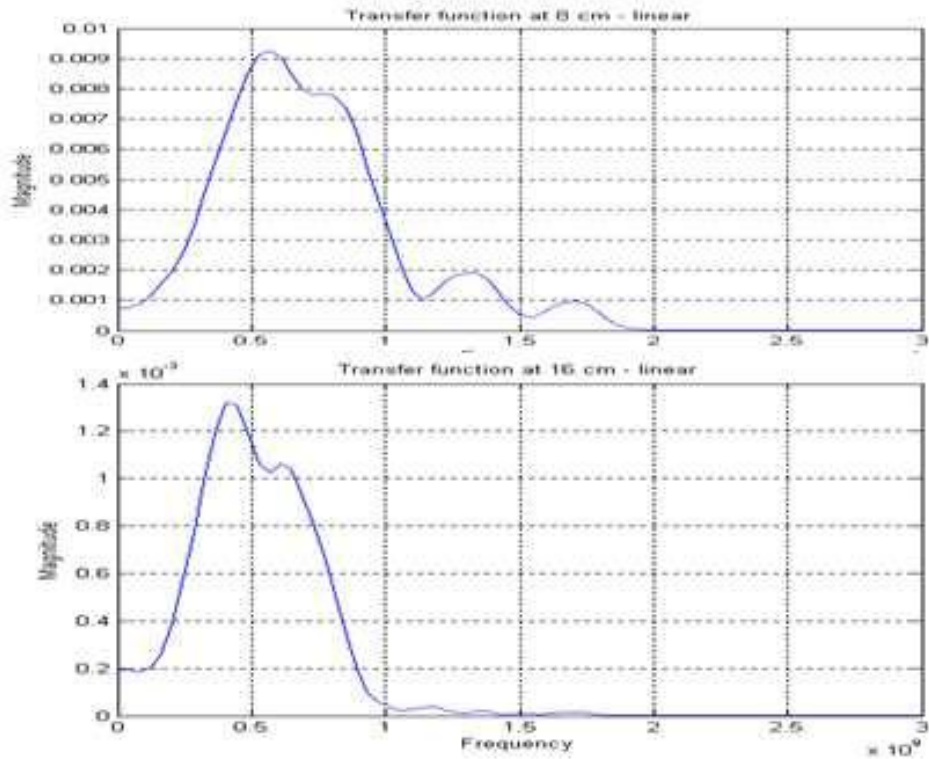


Figure 27: Simulation Bandwidth for distance of 8cm (up) and 16cm (down) inside human body indicating how the operational bandwidth of the FDTD simulation system decreases as distance between the transmitter and receiver antenna increases.

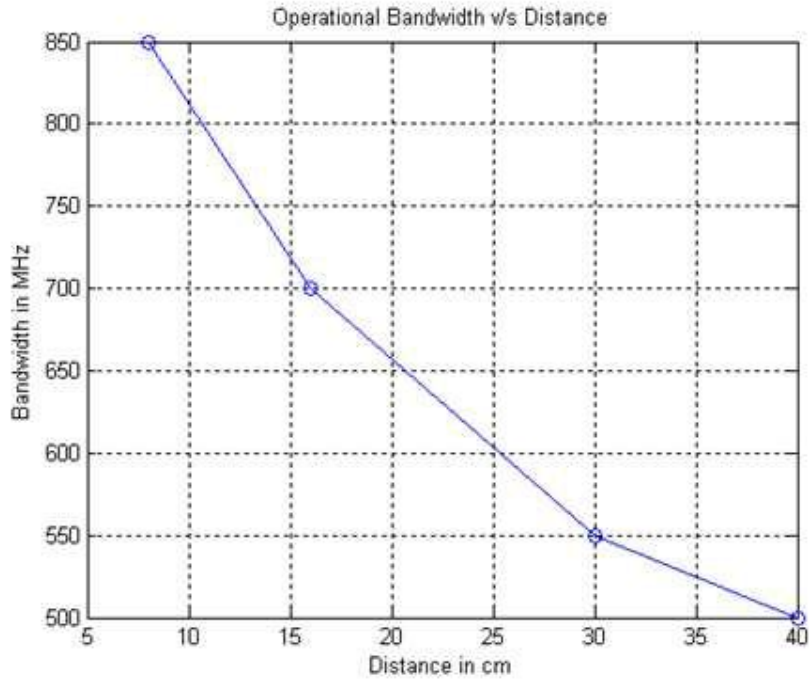


Figure 28: Operational Bandwidth of FDTD vs. distance between the antennas inside homogenous human body

4.6.2 TOA Accuracy as a function of bandwidth

The human body channel suffers from severe multipath propagation and heavy shadow fading conditions so measurement for localization are far from accurate for many instances. Here we try to find the TOA localization accuracy and not RSS. As pointed out in [75], TOA measurements are more accurate than that by RSS. To examine the application of waveform transmission inside human body using FDTD simulations, we determined the statistics of the distance measurement errors using TOA of the received waveform in the scenario shown in Figure 26. The TOA of the signal between the different points in the simulation scenario were calculated for different waveforms using the impulse response of the channel. For TOA based ranging, propagation velocity v , inside human body is expressed as a function of the relative permittivity as shown in the equation 4.8:

$$v(\omega) = \frac{c}{\sqrt{\varepsilon_r(\omega)}} \quad 4.8$$

Where ω is the operating frequency. And c is the velocity in free space. Here we considered $\varepsilon_r = 50$, which is the average permittivity of all the tissue and organs. We use two different waveforms for different localization techniques. First we use a sinusoidal signal, representing narrow band transmission of signal, and use the phase information of the received sinusoidal signal to measure the distance and compared that with the actual physical distance to determine the distance measurement error for TOA estimation. Then we repeat the experience for the wideband pulse transmission by detection of the peak of the received signal for TOA estimation. The statistics of the distance measurement errors obtained from the two experiences for TOA estimation using the narrowband and wideband signals is shown in Figure 29 and 30. The localization error of the narrowband simulation is 0.673 cm compared with the error of the wideband simulation, which is 0.2478 cm. This simple experiment reveals the usefulness of the approach described in this part of thesis. All the results obtained are using the LTI interpretation of the FDTD simulations and the calculation time was negligible with respect to hours of computations needed for the direct simulation of the waveforms. All the above simulations were carried using homogenous human body model. The future work in this area is to use a non-homogenous human body model and using LTI interpretation of the FDTD for analysis of TOA ranging inside human body. In case of non-homogenous human body model, the path traversed by the signal would go through different organs with different permittivity.

$$\bar{v} = \frac{c}{\sqrt{\bar{\varepsilon}_r}} \quad 4.9$$

$$\hat{d} = \hat{t} \cdot \bar{v} = (\hat{t}_1 + \hat{t}_2 + \hat{t}_3 + \dots + \hat{t}_n) \frac{c}{\sqrt{\bar{\varepsilon}_r}} \quad 4.10$$

$$\sum_{i=1}^n \frac{d_i}{v_i} \frac{c}{\sqrt{\epsilon_r}} = \left(\frac{d_1}{\frac{c}{\epsilon_1}} + \frac{d_2}{\frac{c}{\epsilon_2}} + \frac{d_3}{\frac{c}{\epsilon_3}} + \dots + \frac{d_n}{\frac{c}{\epsilon_n}} \right) \frac{c}{\sqrt{\epsilon_r}} \quad 4.11$$

Each organ has different characteristics of conductivity and relative permittivity. The current literature suggests using average permittivity of human body to estimate the average propagation velocity inside human body as shown in equation 4.10 and 4.11. [79][80]:

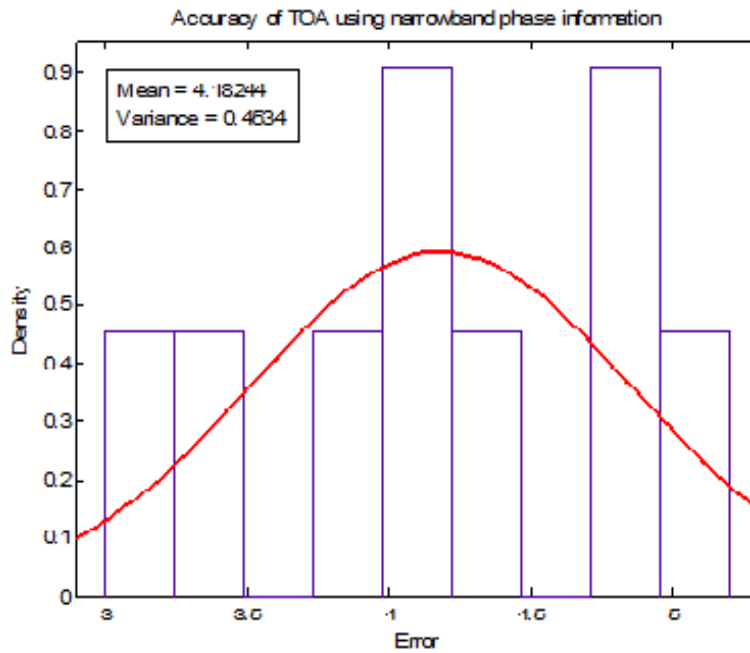


Figure 29: TOA accuracy for narrow band signal for in-body localization using homogenous human body model

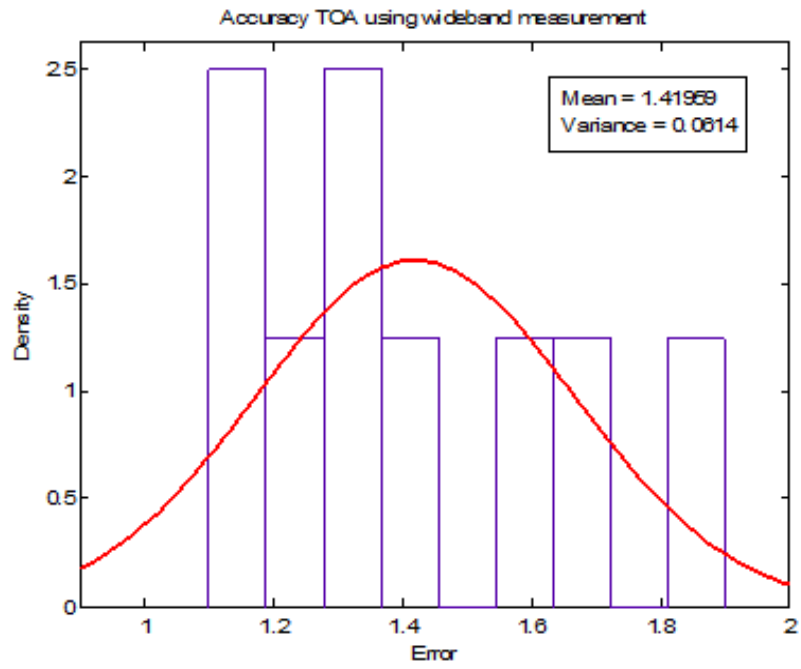


Figure 30: TOA accuracy for Wideband signal for in-body localization using homogenous human body model

Chapter 5

Conclusion and Future Work

In this research, we first derived the accuracy bounds for localization of a capsule inside the human body with an array of sensors located on the surface of human body using an RSS based triangulation algorithm and a surface-to-implant path loss model. We considered the situation where the transmitted powers from the antennas of all the sensors are considered random. Various reasons for randomness in transmit power were highlighted. This scenario more closely represents the situation which occurs in practice for BAN application such as wireless capsule endoscopy. The Bayesian Cramér–Rao bounds were derived in 3D and simplified to matrix form so as to be used for any form of sensor configurations. After analyzing bounds in different organs (small intestine, stomach, large Intestine) and with different number of sensors, it was observed that the large intestine is a harsher implant environment for RF localization, requiring a greater number of receiver sensors on the body surface to achieve the same localization performance as that of the stomach or small intestine. Simulation results show that in general, the

accuracy of location estimation increases greatly when the number of sensors is increased. Yet, the localization error is rather high on the order of few cm, for a reasonably-sized sensor array placed on the surface of the human body for localization of an implant inside the human body using RSS based localization techniques. Hence we resort to TOA based localization.

Due to lack of a widely accepted model for TOA based localization inside the human body we used computational techniques such as FDTD for simulation of propagation inside and around the human body. The FDTD method is a popular numerical method to solve Maxwell's equations in the time domain. We first discussed FDTD in detail along with the associated issues, such as numerical stability, numerical dispersion and the absorbing boundary conditions. From this discussion it is seen that the inherent recursive feature of the FDTD method and the requirement for absorbing boundary conditions are the main shortcomings of this method and make its application limited to electrically small to medium structures. The computational complexity of the FDTD algorithm was studied and was observed that computation time increases as a cubic power of the decrease in grid size. To overcome these limitations, we brought a new perspective to the FDTD algorithm by looking at it as a LTI system. As a result, the simulation time is reduced to just the convolution of input signal with the impulse response of the simulation system.

We first compared the empirical measurements with our proprietary simulation software to check the fidelity of the software using a hollow phantom. Initially, a few weeks were spent calibrating the simulation for a free space scenario so that it could be compared to actual measurements. The measurements were made on a network analyzer that makes frequency domain calculations, whose inverse Fourier Transforms are used to plot the impulse response of the channel. It was observed that the simulation results correspond very accurately with the

measurements made using the vector network analyzer. Then we went ahead in finding the performance of in-body localization using this simulation software. We used the above described method for simulation using FDTD for narrowband and wideband signals. The study conducted in this research verifies that Time of Arrival is a more accurate measure of distance between two sensors in a fading environment than is the Received Signal Strength.

The Future work in this area would be to try to use a non-homogeneous human body model to take into account the multipath characteristics of the human body. With a non-homogeneous human body model, the propagation takes place through different organs with different values of dielectric constants and conductivity, and we can see the true multipath effects of the human body. Currently we are doing research using professional software named SEMCADX which has various human body models to the detail of less than mm level accuracy with different organs inside. We also propose further development of TOA based algorithms for more accurate localization inside the body and exploration of other localization techniques such as AOA.

References

- [1] Benoît Latré , Bart Braem , Ingrid Moerman , Chris Blondia and Piet Demeester “A Survey on Wireless Body Area Networks” *Wireless Networks*, Volume 17 Issue 1, Pages 1-18, January 2011
- [2] B. Heile, “IEEE 802.15 TG 6 PAR,” IEEE15-07-0575/r9, IEEE-SA, December 2007.
- [3] D. Lewis, “802.15 TG 6 Call for Applications – Response Summary,” IEEE15-08-0407r6, IEEE-SA, July 2008.
- [4] A. Astrin, “802.15 TG 6 Call for Proposals (CFP),” IEEE15-08-0829r1, IEEE-SA, November 2008.
- [5] A. Milenkovic, C. Otto, and E. Jovanov, “Wireless sensor networks for personal health monitoring: Issues and an implementation,” *Computer Communications, Wireless Sensor Networks and Wired/Wireless Internet Communications*, vol. 29, no. 13-14, pp. 2521-2533, August 2006.
- [6] I. Chlamtac, M. Conti, and J. Liu, “Mobile ad hoc networking: imperatives and challenges.” *Ad Hoc Networks*, vol. 1, no. 1, pp. 13-64, 2003.
- [7] R. C. Shah and M. Yarvis, “Characteristics of on-body 802.15.4 networks,” in *Wireless Mesh Networks, 2006. WiMesh 2006. 2nd IEEE Workshop on*, Reston, VA, USA, 2006, pp. 138-139.
- [8] Kamyar Yekkeh Yazdandoost, Kamran Sayrafian-Pour, Wen-Bin Yang, John Hagedorn and Judith Terrill, *A Statistical Path Loss Model for Medical Implant Communication Channels*, 2009
- [9] K. Sayrafian-Poue, W. B. Yang, J. Hagedorn, J. Terrill, and K. Yazdandoost, “A statistical path loss model for medical implant communication channels,” in *IEEE 20th International*

Symposium on Personal, Indoor and Mobile Radio Communications, 2009, 13-16 Sept 2009, pp. 2995–2999.

[10] Bardia Alavi, “Distance Measurement Error Modeling for Time-of-Arrival Based Indoor Geolocation”, PhD 2006

[11] IEEE 802.15 WPAN™ Task Group 6 (TG6) Body Area Networks
<http://www.ieee802.org/15/pub/TG6.html>

[12] P. Bergamo and G. Mazzini, “Localization in sensor networks with fading and mobility,” in *The 13th IEEE International Symposium on Personal, Indoor and Mobile Radio Communications*, vol. 2, 2002, pp. 750–754.

[13] E. Elnahrawy, X. Li, and R. Martin, “The limits of localization using signal strength: a comparative study,” in *First Annual IEEE Conference on Sensor and Ad-hoc Communications and Networks*, 2004, pp. 406–414.

[14] D. Madigan, E. Elnahrawy, R. Martin, W.-H. Ju, P. Krishnan, and A. Krishnakumar, “Bayesian indoor positioning systems,” in *IEEE INFOCOM 2005*, vol. 2, 2005, pp. 1217–1227.

[15] D. Niculescu and B. Nath, “Localized positioning in ad hoc networks,” in *IEEE International Workshop on Sensor Network Protocols and Applications*, 2003, pp. 42–50.

[16] N. Patwari, A. Hero, M. Perkins, N. Correal, and R. O’Dea, “Relative location estimation in wireless sensor networks,” *IEEE Transactions on Signal Processing*, vol. 51, no. 8, pp. 2137–2148, 2003.

[17] T. S. Rappaport, *Wireless Communications: Principles and Practice*, 2nd ed. Prentice Hall PTR, 2001.

- [18] D. C. Cox, R. Murray, and A. Norris, "800mhz attenuation measured in and around suburban houses," *AT & T Bell Laboratory Technical Journal*, vol. 673, no. 6, pp. 921–954, 1984.
- [19] R. Bernhardt, "Macroscopic diversity in frequency reuse radio systems," *IEEE Journal on Selected Areas in Communications*, vol. 5, no. 5, pp. 862–870, 1987.
- [20] G. Carter, *Coherence and Time Delay Estimation*. Piscataway, NJ: IEEE Press, 1993.
- [21] C. Knapp and G. Carter, "The generalized correlation method for estimation of time delay," *IEEE Transansaction on Acoustics, Speech, Signal Processing*, vol. 24, no. 4, p. 320327, 1976.
- [22] J.-Y. Lee and R. Scholtz, "Ranging in a dense multipath environment using an UWB radio link," *IEEE Journal on Selected Areas in Communications*, vol. 20, no. 9, pp. 1677–1683, 2002.
- [23] S. Gezici, Z. Tian, G. Giannakis, H. Kobayashi, A. Molisch, H. Poor, and Z. Sahinoglu, "Localization via ultra-wideband radios: a look at positioning aspects for future sensor Networks," *IEEE Signal Processing Magazine*, vol. 22, no. 4, pp. 70–84, 2005.
- [24] G. Carter, "Time delay estimation for passive sonar signal processing," *IEEE Transactions on Acoustics, Speech, and Signal Processing*, vol. 29, no. 3, pp. 463–470, 1981.
- [25] W. A. Gardner and C. K. Chen, "Signal-selective time-difference-of-arrival estimation for passive location of man-made signal sources in highly corruptive environments. i. theory and method," *IEEE Transactions on Signal Processing*, vol. 40, no. 5, pp. 1168–1184, 1992.
- [26] T. Rappaport, J. Reed, and B. Woerner, "Position location using wireless communications on highways of the future," *IEEE Communications Magazine*, vol. 34, no. 10, pp. 33–41, 1996.

- [27] Kaveh Pahlavan and Allen H. Levesque, *Wireless Information Networks*, 2 Edition, Wiley Interscience, 2005.
- [28] Kaveh Pahlavan, P. Krishnamurthy and J. Beneat, "Wideband Radio Propagation Modeling for Indoor Geolocation Applications", *IEEE Communications Magazine*, April 1998.
- [29] Bardia Alavi and Kaveh Pahlavan, "Modeling of the TOA based Distance Measurement Error Using UWB Indoor Radio Measurements" *IEEE Communications Letters*, April 2006.
- [30] Ruijun Fu, Yunxing Ye, Kaveh Pahlavan and Ning Yang , "Doppler Spread Analysis of Human Motions for Body Area Network Applications" submitted to the 22nd Annual IEEE international symposium on personal, indoor and mobile radio communications PIMRC 2011, 11-14 September , Toronto, Canada.
- [31] A. Fort, C. Desset, J. Ryckaert, P. De Doncker, L. Van Biesen, and P. Wambacq, "Characterization of the ultra-wideband body area propagation channel," in *Ultra Wideband*, 2005. ICU 2005. 2005 IEEE International Conference on, Sep. 2005.
- [32] M. Di Renzo, R. M. Buehrer, and J. Torres, "Pulse shape distortion and ranging accuracy in uwbbased body area networks for full body motion capture and gait analysis," in *IEEE Globecom 2007*, November 2007, pp. 3775 - 3780.
- [33] D. Neiryneck, "Channel characterization and physical layer analysis for body and personal area network development," Ph.D. dissertation, University of Bristol, UK, November 2006.
- [34] A. Ylisaukko-oja, E. Vildjiounaite, and J. Mantyjarvi, "Five-point acceleration sensing wireless body area network design and practical experiences," *iswc*, vol. 00, pp. 184- 185, 2004.
- [35] Takahiro Aoyagi, Jun-ichi Takada, Kenichi Takizawa, Norihiko Katayama, Takehiko Kobayashi, Kamyar Yazdandoost, Huan-bang Li and Ryuji Kohno, *Channel models for wearable and implantable WBANs*, July 2008

- [36] L. Roelens, S. Van den Bulcke, W. Joseph, G. Vermeeren and L. Martens, *Path loss model for wireless narrowband communication above flat phantom*, August 2005
- [37] K. Pahlavan, Nonlinear quantization and multi-level/phase modulation and coding, *IEEE Trans. Commun.*, (1991).
- [38] K. Pahlavan, P. Krishnamurthy and J. Beneat, "Wideband radio channel modeling for indoor geolocation applications", *IEEE Commun. Mag.*, 36(4), 60-65(1998).
- [39] B. Alavi, K. Pahlavan, N. Alsindi, and X. Li, "Using UWB Measurements for Statistical Analysis of the Ranging Error in Indoor Multipath Environment," accepted for publication in *International Journal of Wireless and Optical Communications (IJWOC)*, 2006.
- [40] B. Alavi and K. Pahlavan, Modeling of the TOA based Distance Measurement Error Using UWB Indoor Radio Measurements, *IEEE Communication Letters*, Vol. 10, No. 4, pp: 275-277, April 2006. X. Li and K. Pahlavan, Super-resolution TOA estimation with diversity for indoor geolocation, *IEEE Trans. Wireless Communication*, December. 2003.
- [41] Karargyris, A. and Bourbakis, N. "Wireless Capsule Endoscopy and Endoscopic Imaging: A Survey on Various Methodologies Presented" *Engineering in Medicine and Biology Magazine*, IEEE , Volume: 29 , Issue: 1 , Jan.-Feb. 2010, Page(s): 72 - 83
- [42] S. Parker, T. Tong, S. Bolden, and P. Wingo, "Cancer stastics 1997," *CA Cancer J Cinicians*, vol. 47, pp. 5-27, 1997.

- [43] J. D. Levy, R. Shreiber, A. Glukhovsky, and D. Fisher, "Localization of the given m2a ingestible capsule in the given diagnostic imaging system," *Gastrointestinal Endoscopy*, vol. 55, no. 2, pp. 244–254, March 2002.
- [44] J. Oh, S. Shah, X. Yuan, and S. J. Tang, "Automatic classification of digestive organs in wireless capsule endoscopy," in *The 22nd Annual ACM symposium on applied computing*, 2007.
- [45] M. Frisch, A. Glukhovsky, and D. Levy, "Array System and Method for Locating an in Vivo Signal Source," Patent US2002/0 173 718, May 20, 2002.
- [46] M. Fischer, R. Schreiber, D. Levi, and R. Eliakim, "Capsule Endoscopy: the Localization System," *Gastrointestinal endoscopy clinics of north america*, vol. 14, pp. 25–31, 2004.
- [47] K. Arshak and F. Adepaju, "Capsule Tracking in the GI Tract: A Novel Microcontroller Based Solution," in *IEEE sensors applications symposium*, 2006, pp. 186–191.
- [48] M. Kawasaki and R. Kohno, "A TOA Based Positioning Technique of Medical Implanted Devices," in *Third international Symposium on Medical information & communication technology, ISMCIT09*, Montreal, 2009.
- [49] X. Wang, M. Meng, and C. Hu, "A Localization Method Using 3-axis Magnetoresistive Sensors for Tracking of Capsule Endoscope," in *Proc. of IEEE/EMBS*, Soul, 2006, pp. 2522–2525.
- [50] C. Hu, M. Meng, and M. Mandal, "The Calibratio of 3-axis Magnetic Sensor Array System for Tracking Wireless Capsule Endoscope," in *IEEE/RSJ International conference on robots and systems*, 2006, pp. 162–167.

- [51] J. Bulat, K. Duda, M. Duplaga, R. Fraczek, A. Skalski, M. Socha, P. Turcza, and T. Zielinski, "Data Processing Tasks in Wireless GI Endoscopy: Image-based Capsule Localization and Navigation with Video Compression," in *Proc. of IEEE/EMBS*, 2007, pp. 2815–2818.
- [52] R. Kuth, J. Reinschke, and R. Rockelein, "Method for Determining the Position and Orientation of an Endoscopy Capsule Guided Through an Examination Object by Using a Navigating Magnetic Field Generated by Means of a Navigation Device," Patent US2007/0 038 063, February 15, 2007.
- [53] S. Thomas, "Smartpill Redefines 'Noninvasive'," in *Buffalo physician*, vol. 40, 2006, pp. 13–14.
- [54] J. H. D. Levy, R. Shreiber, A. Glukhovsky, and D. Fisher, "Localization of the Given M2A Ingestible Capsule in the Given Diagnostic Imaging System," in *Gastrointestinal Endoscopy*, vol. 55, 2002, p. AB135.
- [55] L. Wang, C. Hu, L. Tian, M. Li, and M. Q. H, "A Novel Radio Propagation Radiation Model for Localization of the Capsule in GI Tract," in *IEEE international conference on robotics and biomimetic*, December 19-23, 2009.
- [56] K. Arshak and F. Adepoju, "Adaptive linearized methods for tracking a moving telemetry capsule," in *IEEE international symposium on industrial electronics (ISIE)*, June 2007, pp. 4–7.
- [57] K. Sayrafian-Pour, W.-B. Yang, J. Hagedorn, J. Terrill, and K. Yazdandoost, "A statistical path loss model for medical implant communication channels," in *Personal, Indoor and Mobile Radio Communications, 2009 IEEE 20th International Symposium on*, 13-16 2009, pp. 2995 –2999.

- [58] Y. Wang, R. Fu, Y. Ye, K. Umair, and K. Pahlavan, "Performance Bounds for RF Positioning of Endoscopy Camera Capsules," in *IEEE Radio and Wireless week*, Phoenix, Arizona, 2011.
- [59] N. Alsindi and K. Pahlavan, "Cooperative localization bounds for indoor ultra-wideband wireless sensor networks," *EURASIP J. Adv. Signal Process*, vol. 2008, pp. 125:1–125:13, January 2008. [Online]. Available: <http://dx.doi.org/10.1155/2008/852509>
- [60] N. Bargshady, K. Pahlavan, Y. Ye, F. Akgul, and N. Alsindi, "Bounds on Performance of Hybrid WiFi-UWB Cooperative Localization for Robotic Applications," in *Proceedings of IEEE International Symposium on Personal, Indoor and Mobile Radio Communications (PIMRC10)*, 2010.
- [61] N. Patwari and A. O. H. III, "Signal strength localization bounds in ad hoc and sensor networks when transmitted powers are random," in *4th Annual IEEE Workshop on Sensor Array and Multichannel Processing*, 2006. WCNC 2009, vol. 1, 12–14 July 2006, pp. 299 – 303.
- [62] H.-B. Li, K. Y. Yazdandoost, and B. Zhen, "Wireless Body Area Network". River Publishers, 2010.
- [63] Pranay Swar, Yunxing Ye, Kaveh Ghaboosi, Kaveh Pahlavan, "On Effect of Transmit Power Variance on Localization Accuracy in Wireless Capsule Endoscopy", *IEEE WCNC*, Paris, France, April 2-5, 2012
- [64] H. Trees, *Detection, Estimation, and Modulation Theory*. John Wiley and Sons, 1968.
- [65] "Ansoft full-wave electromagnetic field simulation," in <http://www.ansoft.com/products/hf/hfss/>.
- [66] A. Taflove and S. C. Hagness, *Computational Electrodynamics: The Finite-Difference Time-Domain Method*, Third Edition, 3rd ed. Artech House, 2005.

- [67] K. Yee, "Numerical solution of initial boundary value problems involving maxwell's equations in isotropic media," in IEEE Transactions on Antennas and Propagation, vol. 14, May 1966, pp. 302–307.
- [68] W. G. Scanlon, J. B. Burns, and N. E. Evans, "Radio wave propagation from a tissue implanted source at 418 MHz and 916.5 MHz," in IEEE Transactions on Biomedical Engineering, vol. 47, 2000, pp. 527–534.
- [69] L. C. Chiwra, P. A. Hammond, S. Roy, and D. R. S. Cumming, "Electromagnetic radiation from ingested sources in the human intestine between 150 mhz and 1.2 ghz," in IEEE Transactions on Biomedical Engineering, vol. 50, 2003, pp. 484–492.
- [70] W. Buchanan, N. Gupta, and J. Arnold, "Simulation of radiation from a microstrip antenna using three-dimensional finite-difference time-domain (fdtd) method," in 8th International Conference on Antennas and Propagation, vol. 50, 1993, pp. 639–642.
- [71] B. Steinhaus, R. Smith, and P. Crosby, "The role of telecommunications in future implantable device systems," in Annual International Conference of the IEEE on Engineering in Medicine and Biology Society, 1994. EMBC 1994, vol. 2, 1994, pp. 1013 – 1014.
- [72] B. C. Towe, "Passive biotelemetry by frequency keying," in IEEE Transactions on Biomedical Engineering, vol. BME-33, 1986, pp. 905–909.
- [73] Weili Ma, "Discrete Green's Function Formulation of the FDTD Method and its Application" Department of Electronic Engineering Queen Mary University of London United Kingdom February 2004
- [74] Pranay Swar, Kaveh Pahlavan, and Umair Khan, "Accuracy of Localization System inside Human Body using a Fast FDTD simulation Technique" 6th IEEE International

Symposium on Medical Information and Communication Technology, La Jolla, CA, March, 2012

[75] U. Khan, K. Pahlavan, and S. Makarov, "Comparison of TOA and RSS based techniques for rf localization inside human tissue," in Annual International Conference of the IEEE on Engineering in Medicine and Biology Society, 2011. EMBC 2011, 2011, pp. 5602–5607.

[76] W. G. Scanlon, J. B. Burns, and N. E. Evans, "Radio wave propagation from a tissue implanted source at 418 MHz and 916.5 MHz," in IEEE Transactions on Biomedical Engineering, vol. 47, 2000, pp. 527–534.

[77] Van Damme W, Meessen B, von Schreeb J, Thay Ly H, Thomé J-M, Overtoom R, & Por I (2001) Sotnikum New Deal, the first year. 1-64. Phnom Penh, MSF Cambodia.

[78] A. Taflove and S. C. Hagness, *Computational Electrodynamics: The Finite-Difference Time-Domain Method, 3rd ed.* Norwood, MA: Artech House, 2005

[79] M. Kawasaki and R. Kohno, "A TOA Based Positioning Technique of Medical Implanted Devices," in *Third international Symposium on Medical information & communication technology, ISMCIT09*, Montreal, 2009.

[80] Yunxing Ye, Umair Kahn and Kaveh Pahlavan, "Accuracy Bounds for RSS and TOA based RF localization in capsule endoscopy", Integrating technology and medicine for a healthier tomorrow, EMBC 2011, August 30th-Sept 3rd, 2011, Boston, MA.

Appendix

Matlab code for finding Cramér-Rao Lower bound

```
%function [stdevs, bound, F, avgNeighb] = calcLocalizationCRB(method,  
x, y, blinds, total, channelParam, measMade, d_thr)  
%  
%  
%  
%AUTHOR: 2Dversion - Neal Patwari, npatwari (at) umich (dot) edu,  
April 2004  
%           http://www.engin.umich.edu/~npatwari/  
%  
%3D version modified by Pranay Swar (email: pranay.swar (at) wpi.edu),  
Aug 2011  
%OUTPUTS:  
%  
% bound:      The matrix bound on covariance  
% F:          The fisher information matrix  
%  
%INPUTS:  
%  
% x and y:    Actual coordinate vectors.  The first 'blinds' elements  
are  
%           blindfolded, and the remaining are 'reference' or  
'anchor'  
%           nodes.  x and y must be row vectors.  
% blinds:     Total # of blindfolded devices.  The first 'blinds'  
devices must  
%           be correspond to the blindfolded devices, the rest are  
references.  
% total:      Total # of devices.  
%
```

```

% measMade: Measurement matrix. measMade(i,j)=1 if i and j make a
%           measurement, or =0 if not. Default is all ones. If a
%           scalar is sent for measMade, it is considered to be a
%           radius: if ||z_i-z_j|| < radius, then i and j makes
measurements,
%           otherwise they don't.
%
%
function [stdevs_x, stdevs_y, stdevs_z, bound, F, F_delta, sigz_bar] =
calcLocalizationCRBz(...
    method, x, y, z, blinds, total, channelParam, sigpi, rho, measMade)

method = upper(method);
if (method ~= 'T') & (method ~= 'R') & (method ~= 'Q' & (method ~=
'A')),
    error('Method must be T (TOA), A (AOA), R (RSS), or Q (QRSS)');
end
% 1. For incomplete measurements, use symmetric matrix measMade to
indicate which pairs
%   made measurements (1 for a measurement, 0 for no measurement).
The default
%   is that all pairs made measurements.
%   Or, if measMade is just a scalar distance, consider it to be a
range, all
%   devices within this range radius 'make measurements' and those
outside of
%   the range don't.
if ~exist('measMade'),
    measMade = ones(total);
end
if length(measMade) == 1, % Of course total > 1
    rangeRadiusSqr = measMade^2;
    measMade = zeros(total);
else

```

```

    rangeRadiusSqr = -1; % Key for don't use range radius
end
% 2. For the case of identical channel variation on every link,
%   accept a scalar value for 'channelParam'.
if length(channelParam) == 1,
    channelParam = ones(total).*channelParam; % channel parameter is
channelParam = sigma/np
end
%   Otherwise, use a channel parameter matrix (only the lower
triangle is
%   used)
if (method == 'T') | (method == 'A'),
    sigmaConst = channelParam; % standard deviation of measured
distance or angle error
elseif (method == 'R') | (method == 'Q'),
    sigmaConst = channelParam.*(log(10)/10); % 1/sqrt(b), where 'b'
is the constant in [1]
end

% 3. Calculate the non-diagonal elements of each of the four sub-
blocks of F.
%   Each matrix is a superset of the elements needed in F11, F12, and
F22,
%   the additional terms are needed for the next step.

%rho = 0.704;
conc = (1+rho)/2;
conc2 = (1-rho)*7.85*7.85/2;

for k = 2:total
    e1 = 1:(k-1);
    deltax = x(k) - x(e1); % calculating the non-diagonal elements for
the kth row
    deltay = y(k) - y(e1);
    deltaz = z(k) - z(e1);

```

```

dSqr    = deltax.^2 + deltax.^2+deltaz.^2;
denom(k,el) = dSqr.^2;
denom1(k,el) = dSqr;

if rangeRadiusSqr > 0,
    measMade(k,el) = (dSqr <= rangeRadiusSqr);
end

frontTerm(k,el) = measMade(k,el) ./ (sigmaConst(k,el).^2).*(conc));
frontTerm2(k,el) = measMade(k,el) ./
((sigmaConst(k,el)).*(conc*4.26));

term12(k,el) = frontTerm(k,el) .* deltax.*deltay ./ denom(k,el);
term12(el,k) = term12(k,el)';
term11(k,el) = frontTerm(k,el) .* deltax.*deltax ./ denom(k,el);
term11(el,k) = term11(k,el)';
term22(k,el) = frontTerm(k,el) .* deltax.*deltax ./ denom(k,el);
term22(el,k) = term22(k,el)';
termzz(k,el) = frontTerm(k,el) .* deltax.*deltax ./ denom(k,el);
termzz(el,k) = termzz(k,el)';
termxz(k,el) = frontTerm(k,el) .* deltax.*deltax ./ denom(k,el);
termxz(el,k) = termxz(k,el)';
termyz(k,el) = frontTerm(k,el) .* deltax.*deltax ./ denom(k,el);
termyz(el,k) = termyz(k,el)';
termz3(k,el) = -frontTerm2(k,el) .*deltax.*(0.5) ./ denom1(k,el);
termz3(el,k) = -termz3(k,el)';

term13(k,el) = -frontTerm2(k,el) .*deltax.*(0.5) ./ denom1(k,el);
term13(el,k) = -term13(k,el)';
term23(k,el) = -frontTerm2(k,el) .*deltax.*(0.5) ./ denom1(k,el);
term23(el,k) = -term23(k,el)';
term33(k,el) = measMade(k,el) ./ (4*conc*7.85*7.85);
term33(el,k) = term33(k,el)';

```

```

end

%%%%%%%%%%%%%%%%%%%%%%%%%%%%%%%%%%%%%%%%%%%%%%%%%%%%%%%%%%%%%%%%%%%%%%%%
% Part 2 for the power variance bounds
%%%%%%%%%%%%%%%%%%%%%%%%%%%%%%%%%%%%%%%%%%%%%%%%%%%%%%%%%%%%%%%%%%%%%%%%

for k = 2:total
    e1 = 1:(k-1);

    deltax1 = x(k) - x(e1); % calculating the non-diagonal elements
    for the kth row
        deltax1 = x(k) - x(e1);
        deltay1 = y(k) - y(e1);
        deltaz1 = z(k) - z(e1);

        dSqr = deltax1.^2 + deltay1.^2 + deltaz1.^2;

        if rangeRadiusSqr > 0,
            measMade(k,e1) = (dSqr <= rangeRadiusSqr);
        end

        term12n(k,e1) = 0;
        term12n(e1,k) = term12n(k,e1)';
        term33n(k,e1) = -measMade(k,e1) ./ (4*conc2);
        term33n(e1,k) = term33n(k,e1)';
    end

    %calculate the diagonal elements
    v_zzn = -sum(term33n(:, 1:total));

    % Calculate each term
    X1_diag1 = zeros(1,blinds);

    F11n = term12n(1:blinds, 1:blinds)+ diag(X1_diag1);
    F12n = term12n(1:blinds, 1:blinds)+ diag(X1_diag1);
    F22n = term12n(1:blinds, 1:blinds)+ diag(X1_diag1);

```

```

Fxn = term12n(1:blinds, 1:blinds)+ diag(X1_diag1);
Fyn = term12n(1:blinds, 1:blinds)+ diag(X1_diag1);
Fzn = term12n(1:blinds, 1:blinds)+ diag(X1_diag1);
Fz3n = term12n(1:blinds, 1:blinds)+ diag(X1_diag1);
F13n = term12n(1:blinds, 1:blinds)+ diag(X1_diag1);
F23n = term12n(1:blinds, 1:blinds)+ diag(X1_diag1);
F33n = term33n(1:total, 1:total) + diag(v_zzn);

F13n(1:blinds,1+blinds:total) = term12n(1:blinds, 1+blinds:total);
F23n(1:blinds,1+blinds:total) = term12n(1:blinds, 1+blinds:total);
Fz3n(1:blinds,1+blinds:total) = term12n(1:blinds, 1+blinds:total);

F_delta = [F11n, F12n,Fxn,F13n; F12n',F22n,Fyn,F23n;Fxn',Fyn',
Fzn, Fz3n; F13n',F23n',Fz3n',F33n];

%%%%%%%%%%%%%%%%%%%%%%%%%%%%%%%%%%%%%%%%%%%%%%%%%%%%%%%%%%%%%%%%%%%%%%%%
%
%%%%%%%%%%%%%%%%%%%%%%%%%%%%%%%%%%%%%%%%%%%%%%%%%%%%%%%%%%%%%%%%%%%%%%%%
%

%Forming the priori matrix

X1 = zeros(1,blinds);
X2 = ones(1,total);
X_diag = [X1,X1,X1,X2./sigpi];
Fp = diag(X_diag);

% 4. Calculate the diagonal elements, which are sums of the elements
on each column.
v_xx = sum(term11(:, 1:blinds));
v_xy = sum(term12(:, 1:blinds));
v_yy = sum(term22(:, 1:blinds));
v_xz = sum(termxz(:, 1:blinds));
v_yz = sum(termyz(:, 1:blinds));

```

```

v_zz = sum(termzz(:, 1:blinds));
v_z3 = -sum(termz3(:, 1:blinds));
v_x3 = -sum(term13(:, 1:blinds));
v_y3 = -sum(term23(:, 1:blinds));
v_33 = sum(term33(:, 1:total));

% 5. Combine the two, using only the terms for the blind devices.
F11 = -term11(1:blinds, 1:blinds) + diag(v_xx);
F12 = -term12(1:blinds, 1:blinds) + diag(v_xy);
F22 = -term22(1:blinds, 1:blinds) + diag(v_yy);
Fzz = -termzz(1:blinds, 1:blinds) + diag(v_zz);
Fxz = -termxz(1:blinds, 1:blinds) + diag(v_xz);
Fyz = -termyz(1:blinds, 1:blinds) + diag(v_yz);
Fz3 = termz3(1:blinds, 1:blinds) + diag(v_z3);
F13 = term13(1:blinds, 1:blinds) + diag(v_x3);
F23 = term23(1:blinds, 1:blinds) + diag(v_y3);
F33 = term33(1:total, 1:total) + diag(v_33); %zeros(total,total)+
diag(v_zz); %

F13(1:blinds,1+blinds:total) = term13(1:blinds, 1+blinds:total);
F23(1:blinds,1+blinds:total) = term23(1:blinds, 1+blinds:total);%
removed the -ve sign
Fz3(1:blinds,1+blinds:total) = termz3(1:blinds, 1+blinds:total);

F = [F11, F12,Fxz,F13 ; F12', F22,Fyz, F23;Fxz', Fyz', Fzz, Fz3;
F13',F23',Fz3', F33];

F = F+F_delta+Fp;
%F = F + Fp;

bound = inv(F);

% 6. The location estimate stdev bound: sqrt( var(x) + var(y) ).
stdevs_x = sqrt(diag(bound(1:blinds,1:blinds))) ;

```

```

stdevs_y = sqrt(diag(bound(1+blinds:2*blinds,1+blinds:2*blinds)));
stdevs_z = sqrt(diag(bound(1+2*blinds:3*blinds,1+2*blinds:3*blinds)));
%+diag(bound(1+2*blinds:3*blinds,1+2*blinds:3*blinds))';

sigz_bar = sum(diag(bound(3*blinds+1:end,3*blinds+1:end)));

% 7. Avg number of neighbors: note that only the lower triangle is
%   calculated when using a radius, and self-measurement isn't
allowed,
%   but the matrix should be symmetric.
avgNeighb = sum(sum(tril(measMade,-1)))*2/total;

```